

KETJU – resolving small-scale supermassive black hole dynamics in GADGET-4

Matias Mannerkoski,¹★ Alexander Rawlings,¹ Peter H. Johansson,¹† Thorsten Naab,² Antti Rantala,² Volker Springel,² Dimitrios Irodoutou,¹ Shihong Liao¹

¹ Department of Physics, University of Helsinki, Gustaf Hållströmin katu 2, FI-00014 Helsinki, Finland

² Max-Planck-Institut für Astrophysik, Karl-Schwarzschild-Str 1, D-85748 Garching, Germany

Accepted XXX. Received YYY; in original form ZZZ

ABSTRACT

We present the new public version of the KETJU supermassive black hole (SMBH) dynamics module, as implemented into GADGET-4. KETJU adds a small region around each SMBH where the dynamics of the SMBHs and stellar particles are integrated using an algorithmically regularised integrator instead of the leapfrog integrator with gravitational softening used by GADGET-4. This enables modelling SMBHs as point particles even during close interactions with stellar particles or other SMBHs, effectively removing the spatial resolution limitation caused by gravitational softening. KETJU also includes post-Newtonian corrections, which allows following the dynamics of SMBH binaries to sub-parsec scales and down to tens of Schwarzschild radii. Systems with multiple SMBHs are also supported, with the code also including the leading non-linear cross terms that appear in the post-Newtonian equations for such systems. We present tests of the code showing that it correctly captures, at sufficient mass resolution, the sinking driven by dynamical friction and binary hardening driven by stellar scattering. We also present an example application demonstrating how the code can be applied to study the dynamics of SMBHs in mergers of multiple galaxies and the effect they have on the properties of the surrounding galaxy. We expect that the presented KETJU SMBH dynamics module can also be straightforwardly incorporated into other codes similar to GADGET-4, which would allow coupling small-scale SMBH dynamics to the rich variety of galactic physics models that exist in the literature.

Key words: black hole physics – galaxies: kinematics and dynamics – methods: numerical – software: simulations – software: public release

1 INTRODUCTION

Supermassive black holes (SMBHs) with masses in the range $M_{\bullet} = 10^6$ – $10^{10} M_{\odot}$ are found in the centres of all massive galaxies in the local Universe (e.g. Ferrarese & Ford 2005; Kormendy & Ho 2013). In the Λ CDM model, galaxies grow through mergers and gas accretion (White & Rees 1978; Naab & Ostriker 2017), and this hierarchical growth will thus invariably result in situations with multiple SMBHs in the same galaxy (e.g. Volonteri et al. 2003).

The SMBH merger process proceeds through three main phases (Begelman et al. 1980; Merritt 2013). First, the SMBHs will sink to the centre of the merger remnant due to dynamical friction and will form a bound binary with a semimajor axis of some tens of parsecs, depending on the masses of the SMBHs. In the second phase the SMBH binary will experience complex three-body interactions with individual stars that drain energy and angular momentum away from the binary (Hills & Fullerton 1980). At this stage the additional drag from gas in the form of a circumbinary disc is also expected to impact the evolution of the binary (e.g. Farris et al. 2014; Duffell et al. 2020). In the final third stage the SMBH binary will be driven

to coalesce by gravitational wave (GW) emission at sub-parsec separations (Peters & Mathews 1963).

Although the basic dynamical framework for SMBH merging is rather well understood, there remain several challenges. For example, one of the challenges is to numerically resolve the detailed interactions of the SMBHs and the stellar component that result in SMBH binary scouring and the formation of galactic cores (e.g. Rantala et al. 2018; Nasim et al. 2021). Modelling the evolution of the SMBH binaries is especially challenging in simulations that simultaneously include a gaseous component (e.g. Chapon et al. 2013; Roškar et al. 2015; Capelo et al. 2015), with one option being that one resorts to an approach that involves the use of on-the-fly code switching (Khan et al. 2016, 2018). Another challenge is to provide detailed predictions for the GWs emitted by SMBH binaries that could be observed by instruments such as the ground-based Pulsar Timing Arrays (PTAs, e.g. Arzoumanian et al. 2018) and the future Laser Interferometer Space Antenna (LISA, Amaro-Seoane et al. 2023).

The SMBH merger process has been traditionally simulated using direct summation N -body codes that are well suited for studying collisional stellar systems with typically $N \lesssim 10^6$ particles (e.g. Ebisuzaki et al. 1991; Milosavljević & Merritt 2001; Berczik et al. 2006; Guillardis & Merritt 2008; Khan et al. 2011; Holley-Bockelmann & Khan 2015). The codes employed for these type of simulations typically use sophisticated high-order integration schemes, including in

★ E-mail: matias.mannerkoski@helsinki.fi

† E-mail: peter.johansson@helsinki.fi

some instances also regularisation, which allows low or zero softening for the gravitational interactions involving SMBHs, and thus enables following the evolution of SMBH binaries to very small spatial scales (e.g. Berentzen et al. 2009; Vasiliev et al. 2015; Gualandris et al. 2017, 2022). However, these types of pure N -body codes do not generally include the capability to simulate the dynamics of gas and the associated astrophysical processes, thus limiting the applicability of these codes for a self-consistent treatment of SMBH dynamics in a full galactic environment. Another fundamental limitation of many direct N -body codes is the number of particles, which is typically limited to a few million for most applications, due to the steep scaling of the computational time with particle number, $O(N^2)$. However, this limit is steadily, but slowly, rising with improvements both in the employed software and the available computational resources (e.g. Aarseth 1999; Harfst et al. 2008; Dehnen 2014; Wang et al. 2015, 2020; Rantala et al. 2021).

In recent years there has also been significant progress in simulating the evolution and impact of SMBHs in both galaxy mergers (e.g. Springel et al. 2005; Johansson et al. 2009a,b; Choi et al. 2012) and in a full cosmological setting (e.g. Sijacki et al. 2007; Booth & Schaye 2009; Hirschmann et al. 2014; Sijacki et al. 2015) using initially smoothed particle hydrodynamics (SPH, Springel 2005; Springel et al. 2005) and also later adaptive mesh refinement (Teyssier 2002; Dubois et al. 2012) and moving mesh codes (Springel 2010; Vogelsberger et al. 2013). These simulations allow for a very large number of particles, as the gravitational forces are typically resolved with either a tree or a mesh resulting in a typical scaling of $O(N \log N)$ of the computational time. In addition, these simulation codes are able to model astrophysical processes by including sophisticated subresolution models for gas physics, star formation and the feedback from evolving stellar populations and SMBHs.

However, a fundamental limitation of this approach is the necessary inclusion of a gravitational softening or equivalently a minimum grid cell that sets a natural resolution limit, below which the dynamics cannot be accurately resolved. A possible solution to circumvent the effects of softening is to add a subresolution drag force to the equations of motion to account for the unresolved dynamical friction (Tremmel et al. 2015; Chen et al. 2022; Ma et al. 2023). However, in most applications the merging of SMBHs below the softened resolution limit has instead been modelled using semi-analytic methods (e.g. Kelley et al. 2017a,b; Bonetti et al. 2019; Izquierdo-Villalba et al. 2022), which have to make several assumptions about the unresolved binary orbits.

The hybrid method is an alternative approach that combines the best aspects of direct summation codes and softened galaxy formation codes by linking together the lower-accuracy hydrodynamical galaxy formation codes used for cosmological simulations, such as the various versions of GADGET and related codes, with a more accurate integration scheme used only in the vicinity of SMBHs. This allows for simultaneously modelling global galactic-scale dynamical and astrophysical processes, while solving the dynamics of SMBHs and the surrounding stellar systems at sub-parsec resolution. In addition, a hybrid code enables running isolated galaxy mergers without gas at higher resolution and in greater number than is possible with the more traditional types of direct N -body codes. Several such hybrid codes have been developed, for example Jernigan & Porter (1989) and McMillan & Aarseth (1993) combined a tree code with a regularisation algorithm, whereas Oshino et al. (2011) and Iwasawa et al. (2015) also combined a tree algorithm with a direct summation code, but without the inclusion of regularisation. There are also code frameworks, such as BRIDGE (Fujii et al. 2007) and AMUSE (The Astrophysical Multipurpose Software Environment, Pelupessy et al.

2013) which enable the combination of different types of N -body codes for the same simulation problems. For KETJU the most direct precursor code is the rVINE code (Karl et al. 2015), which combines algorithmically regularised integration with the VINE code, which is a tree/SPH code employing a binary tree algorithm (Wetzstein et al. 2009).

The first version of KETJU (Rantala et al. 2017) was implemented within the GADGET-3 code. This version of the code was used to run isolated collisionless galaxy mergers in order to study the formation of cores in massive galaxies (Rantala et al. 2018, 2019) and for calculating the GW signal from inspiraling SMBHs in galactic-scale simulations (Mannerkoski et al. 2019). The code was subsequently improved, with the main updates including the replacement of the original regularised AR-CHAIN integrator (Mikkola & Merritt 2008) with the MSTAR integrator (Rantala et al. 2020), which resulted in a significant performance improvement. In addition, the code interface was updated, especially as regarding the treatment of hydrodynamics and feedback, thus enabling both cosmological zoom-in simulations with tens of SMBHs (Mannerkoski et al. 2021, 2022) and isolated merger simulations of gas-rich galaxies (Liao et al. 2023), including now also the effects of gas cooling, star formation, stellar feedback and crucially the feedback from SMBH binary systems (Liao et al. 2023).

While the original version of KETJU was implemented in GADGET-3, in this paper we instead discuss a new version of KETJU, as implemented in GADGET-4. Unlike GADGET-3 which was never publicly released, GADGET-4 (Springel et al. 2021) was recently made publicly available. We have thus now implemented the KETJU SMBH dynamics module into GADGET-4 and together with this paper we make this version of KETJU publicly available.¹ In this paper we describe this new public implementation of KETJU and present several tests of code correctness and performance, as well as an example application demonstrating how the KETJU code can be used to simulate complex systems with multiple merging SMBHs.

This paper is structured as follows. In Section 2 we describe the main features of the KETJU code, GADGET-4 and the regularised MSTAR integrator, with a main emphasis on how the interface between the codes operates. In this Section we also present a schematic of how the KETJU integration is performed. In Section 3, we perform various code tests by first demonstrating that KETJU correctly captures dynamical friction and produces converged results in the hardening rate of SMBH binaries. This is followed by integrator tolerance and computational scaling tests. Then, in Section 4 as a KETJU demonstration we perform simulations of multiple merging galaxies containing SMBHs, in order to study the formation of extended galactic cores. Finally, in Section 5 we present our conclusions.

2 CODE DESCRIPTION

2.1 KETJU overview

The main purpose of KETJU is to allow capturing of the small-scale dynamics of SMBHs in large-scale galactic merger and cosmological simulations run with galaxy formation codes, such as GADGET, by introducing a separate higher-accuracy integrator that is used to solve the dynamics in small regions around SMBHs. The integrator used in KETJU utilises algorithmic regularisation (Mikkola &

¹ <https://www.mv.helsinki.fi/home/phjohans/ketju>

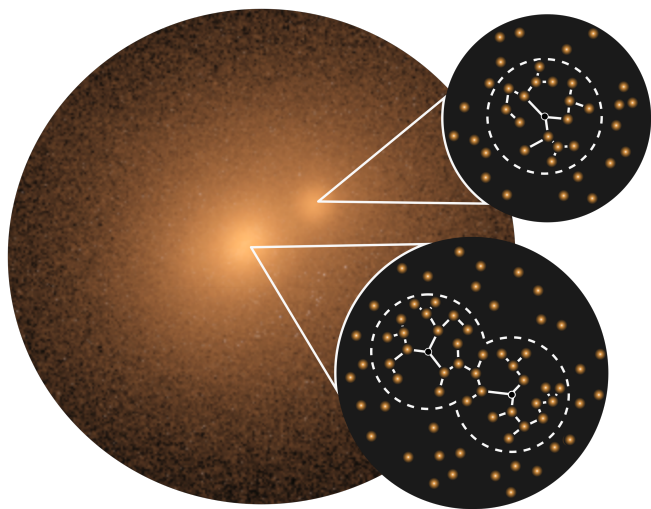


Figure 1. An illustration of KETJU applied to a system of three merging elliptical galaxies, where the first merger has already completed resulting in an SMBH binary, with the third galaxy currently merging into the system. The main idea in KETJU is to add small spherical regions (dashed circles) with typical radii of ~ 10 pc centred on the SMBHs (shown as black dots in the two insets), where the dynamics are integrated using a high-accuracy regularised integrator. This allows treating SMBHs as point particles even in close interactions with other particles, allowing the small-scale dynamics to be modelled below the gravitational softening length used in other parts of the simulation. The surrounding kiloparsec-scale structure of the galaxies, shown in the background image, is simulated using the standard GADGET-4 methods with softened gravity. The regularised integrator uses a minimum spanning tree-based relative coordinate system to reduce rounding errors in close encounters, indicated with the white lines between the particles. The figure is reproduced from [Mannerkoski \(2022\)](#).

[Tanikawa 1999a,b](#)), which enables the integration of close encounters between point masses without running into issues caused by the divergence of the Newtonian gravitational acceleration. This allows modelling gravitational interactions with SMBHs using non-softened gravity, thus overcoming the resolution limitation caused by gravitational softening that is required by the methods used in codes such as GADGET. In addition, the integrator includes post-Newtonian corrections for the interactions between SMBHs, which allows it to directly model the SMBH merger process from the start of a galactic merger down to the few final orbits before the SMBHs coalesce. The main idea of KETJU is depicted in [Figure 1](#).

2.2 GADGET-4

The code presented here extends the public version of GADGET-4, which is described comprehensively by [Springel et al. \(2021\)](#). Here we briefly summarise the main features of GADGET-4 that are relevant for understanding how the KETJU module operates. The modifications added to our KETJU version of GADGET-4 are discussed later in section 2.4.

GADGET-4 is an N -body and hydrodynamics code that includes several methods for calculating gravitational interactions and for integrating the dynamics of particles. Gas dynamics is modelled using smoothed particle hydrodynamics (SPH), and a basic radiative cooling module, star formation and subgrid stellar feedback model ([Springel & Hernquist 2003](#)) are also included. However, the public version of GADGET-4 does not include models for gas accretion

onto SMBHs and the associated feedback, or models for seeding SMBHs in cosmological simulations. Therefore in this paper we only study collisionless KETJU simulation applications without gas. GADGET-4 supports both physical coordinate based simulations of isolated systems and periodic boxes, as well as cosmological simulations using comoving coordinates.

The different methods available for calculating gravitational interactions are the one-sided tree-based multipole expansion, and the fast multipole method (FMM), both of which can be paired with a particle mesh (PM) method for faster calculation of long-range interactions. For the one-sided tree method, the particle distribution is divided using an oct-tree, and the acceleration of each particle is calculated by walking this tree from top to bottom. The gravitational acceleration caused by the particles within a tree node is calculated either using a multipole expansion of a set order of the particles within the node, or by recursively considering the child nodes describing smaller volumes of space, depending on an opening criterion with a user-specified accuracy parameter. In the FMM method the tree structure is used similarly, but instead of simply considering particle-node interactions, the method computes multipole expansions for full node-node interactions. This results in symmetric interactions between particles, allowing manifest momentum conservation when paired with a suitable time integration scheme, in contrast to the one-sided tree method which uses asymmetric interactions.

For all gravitational interactions, GADGET-4 uses a spline softening kernel with support within 2.8ϵ , where ϵ is a user-specified Plummer-equivalent softening length, which can be different for different particle types ([Springel et al. 2021](#)). Outside the support of the softening kernel, all interactions are Newtonian.

For time integration, GADGET-4 includes two different schemes, both based on leapfrog integration and a hierarchy of timebins. The first scheme is the traditional nested time integration scheme, which was also used in earlier versions of GADGET ([Springel 2005](#)). In this scheme the particle timesteps Δt are determined based on their accelerations a in the previous timestep and a user-specified accuracy parameter η as

$$\Delta t = \sqrt{\frac{2\eta\epsilon}{|a|}}. \quad (1)$$

The timesteps are then truncated to timestep bins based on a powers-of-two division of the simulation time. When the current simulation time is evenly divided by the stepsize of a given bin, the particles on that bin are said to be active. Gravitational accelerations need to be calculated only for the active particles, but all particles act as sources, requiring the full particle distribution to be included when constructing the oct-tree for gravity calculations. The asymmetric interactions caused by this scheme also result in the non-conservation of momentum in the system.

The second scheme is the hierarchical time integration, based on splitting the Hamiltonian of the system recursively into so-called slow and fast components. The particles are assigned timebins as above, but in this scheme only the active particles are included as sources of gravity. This allows symmetric interactions and manifest momentum conservation when paired with FMM, and can also improve performance for systems where the hierarchy of timebins is deep.

To parallelise calculations, GADGET-4 uses the Message Passing Interface (MPI) to communicate between tasks or processes that are run in parallel on different CPU cores potentially across multiple supercomputer nodes. Each task stores a subset of the simulation

particles and is responsible for evolving them, with the distribution of particles across tasks based on the spatial distribution of particles.

2.3 The regularised integrator

To integrate the dynamics of BHs and their surrounding stellar component, KETJU uses an updated version of the MSTAR integrator (Rantala et al. 2020). MSTAR uses algorithmic regularisation (Mikkola & Tanikawa 1999a,b; Preto & Tremaine 1999), which employs a time transformation to a new time coordinate to allow integrating gravitational interactions without running into numerical issues caused by the diverging Newtonian potential ($\Phi \propto r^{-1}$).

To reduce roundoff error when calculating gravitational interactions between nearby particles, the code also uses a minimum spanning tree-based chained coordinate system (Rantala et al. 2020). In order to achieve tight numerical tolerances while enabling efficient parallelisation to hundreds of CPU cores for systems of thousands of particles the code uses an MPI-parallelised Gragg–Bulirsch–Stoer extrapolation scheme. The accuracy of the integration is controlled with a per-step relative error tolerance parameter, ϵ_{GBS} , and gravitational forces are calculated using direct summation.

Due to the time transformation used in algorithmic regularisation, the physical time t needs to be integrated like other coordinates of the system, and integrating the system over a specified physical time interval Δt requires iteratively changing the stepsize to reach the desired final time. The accuracy of this iterative solution is controlled by the output time relative tolerance parameter ϵ_t , with the iteration ending when the desired tolerance is reached, i.e. when

$$|t - t_0|/\Delta t < \epsilon_t. \quad (2)$$

Compared to the MSTAR version discussed by Rantala et al. (2020), the publicly released version presented here also includes in addition post-Newtonian (PN) dynamics for black holes, mergers of black holes with GW recoil kicks, optional gravitational softening between stellar particles, and dynamic order control.

Dynamic order control allows adjusting the number of different substep divisions used in the Gragg–Bulirsch–Stoer extrapolation algorithm, which improves the efficiency of the code particularly in situations where integrating the system at the desired accuracy does not require a particularly high integrator order, e.g. when a system is integrated for only a small fraction of its relevant dynamical timescales. This dynamic order control is implemented using standard methods (e.g. Hairer et al. 1993, ch. II.9), with some simplifications to allow for computing multiple rows of the extrapolation table in parallel.

The support for PN dynamics and softening divides the particles in the integrator into two types: particles that always behave like point particles and have PN terms in their mutual interactions, which are typically used to represent black holes, and particles that only experience Newtonian gravity and may optionally have softened interactions between each other, which we call stellar particles due to the typical use case. The optional softening between the stellar particles is implemented using the same spline softening kernel as is used in GADGET-4 (Springel et al. 2021), allowing for continuous transition of stellar particles between GADGET-4 and the regularised integrator. The importance of this feature will be demonstrated in Section 3.5. The gravitational softening only affects interactions between stellar particles, and interactions between stellar particles and black holes are always non-softened.

For PN dynamics, the expressions from Thorne & Hartle (1985) are used for the 1PN and spin terms, including all the non-linear

N -body cross-term effects at this order, while higher-order corrections valid for binary systems up to 3.5PN order are adopted from equation (203) of Blanchet (2014). Apart from a quadrupole spin interaction term that is specific for black holes, the PN terms implemented in the code are also valid for other types of compact objects. The code also supports enabling and disabling individual correction terms, so it is possible to run simulations using e.g. only the leading GW radiation reaction term at 2.5PN order while ignoring the other terms, if so desired. To integrate the equations of motion that include velocity dependent accelerations, the code applies the auxiliary velocity scheme (Hellström & Mikkola 2010; Pihajoki 2015), which allows the integration scheme to remain symmetric and the extrapolation algorithm to operate correctly.

As the PN effects allow black hole binaries to shrink due to GW emission, the integrator also now includes a merger model based on the fitting formulae from Zlochower & Lousto (2015), which predicts the black hole merger remnant spin, mass, and recoil velocity relative to the binary rest frame. The binary rest frame is approximated with the 3PN formulae from de Andrade et al. (2001), with the addition of the leading spin-dependent correction (e.g. Keppel et al. 2009). The merger is by default performed when the binary separation is

$$r = 12R_S = 24G(m_1 + m_2)/c^2, \quad (3)$$

where R_S is the Schwarzschild radius corresponding to the total binary mass, $m_{1,2}$ are the masses of the binary components, G is the gravitational constant, and c is the speed of light.

The rather large merger separation is necessary as the PN formulae used in the calculations are only approximations. At smaller separations, first the centre-of-mass formulae used for computing the rest frame begin to become inaccurate, resulting in oscillations of the calculated centre-of-mass velocity and an incorrect final velocity of the merger remnant, while at even smaller separations the acceleration formulae become inaccurate, leading to clearly unphysical behaviour such as binaries reverting back to expansion. The default merger distance of $12R_S$ has been chosen to avoid most of these issues while allowing the majority of the binary inspiral to be captured. The distance is also user-configurable, and values as low as $6R_S$ can work fairly well at least for low-spin systems.

As the binary is merged at a wider separation than the initial condition distance of $\sim 3R_S$ used in deriving the approximate Zlochower & Lousto (2015) fitting formulae, the resulting binary properties cannot be regarded as exact predictions. In addition, the properties of the fitting functions cause the results to oscillate over the range of possible values that can be obtained with a given spin and mass configuration during the orbit of the binary, and thus the results can be regarded as an effectively random sample from the distribution of possible remnant properties.

The integrator code is published in its own repository as a library with a simple interface. In addition to being used in KETJU, it can also be used as a stand-alone code through a simple driver program, or called from other simulation codes. This should allow implementing similar functionality as presented here also in other simulation codes apart from GADGET-4, such as AREPO (Springel 2010), RAMSES (Teyssier 2002) and ENZO (Bryan et al. 2014), by only implementing the interface code needed for passing particle data to and from the integrator in a similar manner as described in the next section.

2.4 Combining GADGET-4 with the regularised integrator

The main addition to the GADGET-4 code required for KETJU is the interface code, which handles passing particle data to and from the integrator, as well as adjusting the leapfrog timesteps assigned

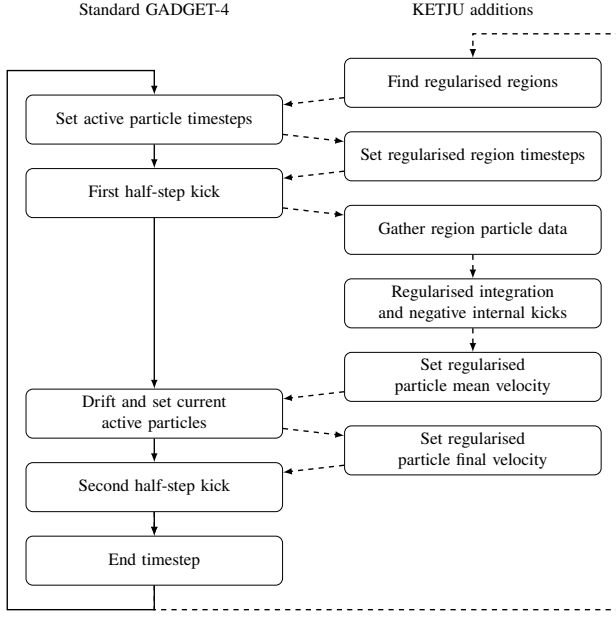


Figure 2. A schematic of the actions performed when integrating over a single leapfrog timestep. The solid lines show the path taken in standard GADGET-4, while the dashed lines show the path taken when the KETJU module is active. The figure is simplified by ignoring some tasks such as output or other additional physics models.

to the particles integrated with the regularised integrator. The main steps in the operation of the code are illustrated in Figure 2.

2.4.1 Finding the regularised regions

On each timestep before the first kick operation, the code first searches for active BH particles and their surrounding stellar particles within a spherical regularised region with a user-specified region radius, r_{region} . The radius of the region must be larger than the softening kernel ($r_{\text{region}} \geq 2.8\epsilon$) in order to ensure that all interactions between BHs and stellar particles are non-softened both inside and outside the regularised regions. Overlapping regions are merged together, so that the spatial extent of each region is a union of spheres, with a BH at the centre of each sphere as depicted in Figure 1. Only active particles are included in the regions, but the following timestep limiting logic aims to ensure that all stellar particles are active when they enter within r_{region} of a BH.

Any other types of particles, such as gas and dark matter (DM), are treated as in standard GADGET-4, even if they are within r_{region} . The code does however include support for treating multiple user-specified types of non-gaseous particles as stellar or BH particles when constructing the regularised regions, as there are no fundamental differences between the different non-gaseous particle types apart from an integer tag in GADGET-4, with the limitation that they must all use the same softening length. This allows for applications where different particle types are used in additional physical models within GADGET-4 to e.g. track newly created stellar particles, or even including DM particles in the regularised regions so that they too can have point-mass interactions with black holes.

The search for particles is implemented in two phases. First each parallel task walks through the particles that are stored in its local

memory to find the BH particles. The BH particle coordinates and other relevant properties are then communicated to all tasks, and each task then checks for each stellar particle in its local memory if it belongs to a region around any of the BHs. The stellar particle data is then communicated between tasks only just before calling the regularised integrator. This simple approach requires only little communication between tasks during this particle search phase, and has shown good performance in our tests, taking in general less than one percent of the total computation time.

2.4.2 Timestep limiting

The timestep determination of the particles within each regularised region is altered to account for the fact that their full dynamics are no longer integrated with the simple leapfrog integrator of GADGET-4. The timestep of each region is set by finding the lowest timestep assigned to a particle within a configurable radius that is set by default to $100r_{\text{region}}$, excluding the particles that belong to the region, and using that as the timestep of the region. This ensures that the internal dynamics of the region are visible to the particles that are directly affected by them. The default size of this timestep limiting radius is set quite conservatively to ensure similar behaviour as earlier versions of KETJU where this limit was imposed based on all particles. However, in general the smallest timesteps are found near the BHs just outside the regularised regions, and the size of this timestep limiting region has little practical impact. In addition to the particles in a regularised region, the stellar particles within a radius of $r < 2r_{\text{region}}$ are also limited to the timestep of the region to ensure that they are active when they enter the region.

Additional limits on the timestep of the region are placed based on the motion of the BHs and stars within the region, to guard against cases where the particle acceleration based timestep limit is not sufficient due to large velocities that would cause particles to pass through the regularised region without being integrated correctly. These limits consist of: (i) the centre of mass (CoM) acceleration limit, evaluated using equation (1) with the softening ϵ replaced by $0.1r_{\text{region}}$; (ii) the CoM velocity v_{CoM} based limit

$$\Delta t \leq \frac{0.1 r_{\text{region}}}{v_{\text{CoM}}}, \quad (4)$$

which ensures that the region does not move too much relative to its size in a single timestep; (iii) the individual BH velocity v_{BH} based limit

$$\Delta t \leq \frac{0.3 r_{\text{region}}}{v_{\text{BH}}}, \quad (5)$$

which ensures that a BH cannot move outside the region during a single step; and finally (iv) a limit based on the stellar velocity dispersion σ

$$\Delta t \leq \frac{r_{\text{region}}}{6\sigma}, \quad (6)$$

which acts to ensure that essentially no stellar particle moves through the region in a single step. The numerical factors in these limits are chosen so that particles that enter a region do not come too close to the central BHs during the final leapfrog step before the regularised integrator takes over, even in the case of fast relative motions. Otherwise, the final half-step kick could be significantly affected by softening and the effect of the BH on the motion of the particle would not be accurately captured. The main timestep criterion based on the surrounding particle timesteps is however what typically sets the timestep, and these limits are only intended

to reduce the impact of the rare cases where it is not sufficient to capture the dynamics.

2.4.3 Integration

The particles in the regularised regions undergo normal leapfrog kicks, but the contributions from the interactions within a given region are then removed by applying additional negative kicks before and after calling the regularised integrator. This avoids the need to modify how the kicks are performed in GADGET-4, while also avoiding double counting the interactions which are already accounted for by the regularised integration. The leapfrog kicks allow including the perturbing effects of the particles that do not belong to the regions at the same level of accuracy as is achieved for the particles integrated by the standard GADGET-4 leapfrog integrator. As the BH particles are in general the most massive particles in the applications KETJU is mainly intended for, the effects of the perturbations on their motion are usually captured even more accurately than this. This is because the region timestep is at least as small as the timesteps of the surrounding perturbing particles, and the acceleration of the massive BH caused by the perturbing particle is smaller than the corresponding acceleration of the much less massive perturbing particle due to the gravity of the BH.

After the first half-step kick has been applied, the particle data is passed to the regularised integrator, and the region is integrated over the leapfrog timestep. However, as algorithmic regularisation is used in the integration, the timespan of the integration will not be exactly equal to the given timestep, and will instead only match it to the tolerance specified by ϵ_t . The integrator output time tolerance parameter ϵ_t must therefore be sufficiently small, so that the error from these slight time differences is not significant compared to the accuracy of the GADGET-4 leapfrog integration. The integration can also be performed in parts to allow for output of the BH data with a time interval that is shorter than the timestep of the region. The BH data is then outputted in HDF5-format after all regions have been integrated.

Different regions are integrated in parallel, with the available MPI tasks allocated between the regions based on the estimated computational cost of each region. The computational cost estimate C is based on the actual measured CPU time taken by the region on the previous timestep, or if not available, on the particle count N_{part} assuming that the $\mathcal{O}(N_{\text{part}}^2)$ gravitational interactions account for the bulk of the cost. Each region is then allocated N tasks so that C/N is approximately equal for all regions, which should minimise the time tasks spend being idle while waiting for other regions to finish their integration. In some cases there may not be enough tasks to integrate all regions in parallel, in which case sets of parallel integrations are queued in sequence so that the total estimated computational time is minimised.

For the integration, the particle data is always converted to physical coordinates in the inertial rest frame of the centre of mass of the region, as the integration scheme adopted in the regularised integrator does not support the comoving integration formalism. This is not an issue for the accuracy of the dynamics even in cosmological simulations, as compared to using comoving integration, performing the integration in physical coordinates without additional correction terms only ignores the effect of the cosmological constant or alternatively dark energy during the integration. For typical systems that KETJU might be applied to in a cosmological context, this ignored contribution is much smaller than other sources of error in the system, such as the integration error or not including the PN terms in all inter-

actions. The inertial frame of the region is drifted over the leapfrog timestep similarly to a simulation particle, i.e. either in physical or comoving coordinates as required by the type of the simulation.

In some cases, the computational cost of the regularised integration can be significantly increased by the formation of very tight binaries, which may not be of physical interest in all cases. One such case is the typical configuration in galactic simulations, where individual stellar particles have masses of around $10^5 M_\odot$, and the rare sub-parsec scale binaries they may form with an SMBH do not meaningfully affect the dynamics of the system, at least when compared to the computational effort needed to integrate them.

To reduce the performance impact of such binaries, the code can optionally add an artificial kick that expands the tightest binary in the system if it has a short enough period to affect the integration performance, excluding of course any SMBH binaries that are always physically meaningful. The kick is applied before the integration, and its magnitude is chosen so that the period of the binary is doubled. Application of such artificial kicks naturally breaks the conservation of energy in the system, so the choice of using this mechanism depends on the desired balance of performance and accuracy. We enable this artificial expansion of tight binaries for our tests presented in this paper, without any apparent impact on the physical results. Other authors have also applied similar schemes to reduce the impact of such unimportant tight binaries, for example [Milosavljević & Merritt \(2001\)](#) directly removed such stellar particles from their simulation.

After the integration, the data in the integrator structures represents the resulting particle state at the end of the timestep at time $t + \Delta t$, but GADGET-4 has only completed the first kick operation of this timestep. To update the GADGET-4 data for the particles in the regularised regions, the final particle velocities are first stored in a separate field, while the velocity field of each particle in the GADGET-4 particle data is set to a mean velocity

$$\mathbf{v}_{\text{mean}} = \frac{\mathbf{x}(t + \Delta t) - \mathbf{x}(t)}{\Delta t} \quad (7)$$

that results in the particle arriving at the correct final position $\mathbf{x}(t + \Delta t)$ at the end of the leapfrog drift step. This avoids the need to modify the GADGET-4 drift routine to check which particles have been integrated with the regularised integrator. After GADGET-4 has performed the drift step, the velocity field of the particles is updated to the correct final velocity $\mathbf{v}(t + \Delta t)$.

2.4.4 Interaction with different GADGET-4 modes

The operation of the interface code is essentially the same in both time integration modes available in GADGET-4. It can however be better theoretically justified in the hierarchical time integration mode, where the regularised regions behave essentially like additional fast systems with the leapfrog evolution replaced by the more accurate regularised integration. So instead of the evolution operator of equation (50) of [Springel et al. \(2021\)](#)

$$\begin{aligned} E(H, \Delta t) \simeq & K_P^P \left(\frac{\Delta t}{2} \right) K_F^F \left(-\frac{\Delta t}{2} \right) \\ & \times E \left(H_F, \frac{\Delta t}{2} \right) D_S(\Delta t) E \left(H_F, \frac{\Delta t}{2} \right) \\ & \times K_F^F \left(-\frac{\Delta t}{2} \right) K_P^P \left(\frac{\Delta t}{2} \right), \end{aligned} \quad (8)$$

where K and D are the kick and drift operations, and $P = S + F$ is the set of particles split into slow (S) and fast (F) systems, we now have

$$E(H, \Delta t) \simeq K_P^P \left(\frac{\Delta t}{2} \right) K_R^R \left(-\frac{\Delta t}{2} \right) \times D_S(\Delta t) E_R(\Delta t) \times K_R^R \left(-\frac{\Delta t}{2} \right) K_P^P \left(\frac{\Delta t}{2} \right), \quad (9)$$

where E_R is the evolution of the regularised region particles (R) implemented by the regularised integrator. Note that here D_S and E_R commute, so that $D_S(\Delta t) E_R(\Delta t) = E_R(\Delta t/2) D_S(\Delta t) E_R(\Delta t/2)$.

An important difference to the hierarchical leapfrog integration is however the fact that the different regularised regions do not interact with each other during the regularised integration, whereas in the hierarchical leapfrog integration all particles at a given level interact with each other. However, due to the timestep limitations, the interaction between nearby but separate regularised regions is accounted for at a sufficient level of accuracy by the perturbing leapfrog kicks.

The different gravity calculation modes also do not affect the operation of the interface code, as they only change how the acceleration entering the leapfrog kicks is calculated in GADGET-4. In principle the different modes might produce slightly different results for the gravitational accelerations caused by interactions within a region, which are then removed by applying additional negative kicks, but this is not accounted for in the interface code, which always uses direct summation for calculating these negative kicks. However, this is not an issue, as all the gravity calculation modes behave like direct summation on the scales that are typical for the regularised regions. The choice of the gravity algorithm and time integration mode can therefore be based on their different strengths.

For the types of simulations that KETJU is particularly well suited for, the momentum conservation and better handling of deep timestep hierarchies given by the combination of hierarchical time integration and FMM gravity seems to make it the preferred default choice. Note however that some momentum non-conservation is introduced into the simulation by the regularised integrator, most importantly through the physical effects of GW emission included in the PN equations of motion and the BH merger model, and to a lesser degree due to numerical errors as the regularised integration scheme is not manifestly momentum conserving.

3 CODE TESTS

3.1 Code settings

We run all the code tests and example applications on the Mahti supercomputer hosted by CSC – IT Center for Science, Finland. The main CPU nodes of Mahti have two AMD Rome 7H12 CPUs with 64 cores each, and 256 GB of memory. For most runs we use just a single node.

Unless otherwise noted, we use an error tolerance of $\epsilon_{\text{GBS}} = 10^{-8}$ and an output time tolerance of $\epsilon_t = 10^{-6}$ for the regularised integration. For gravity calculations in GADGET-4, we use FMM with second order multipoles, a force error tolerance of $\alpha = 0.005$ and an integration error tolerance of $\eta = 0.002$. The runs are performed using the hierarchical integration mode of GADGET-4. When analysing orbits of SMBH binaries, we use the quasi-Keplerian PN orbital elements of Memmesheimer et al. (2004), as described in Mannerkoski et al. (2019).

3.2 Dynamical friction in a Plummer sphere

In order to demonstrate that the new implementation of KETJU in GADGET-4 correctly captures the dynamical friction on BHs from stellar particles, we simulate the orbital decay of an $M_\bullet = 10^8 M_\odot$ SMBH on a circular orbit in a spherical galaxy model. The model consists of only stellar particles distributed according to a Plummer density profile

$$\rho(r) = \frac{3M}{4\pi r_s^3} \left(1 + \frac{r^2}{r_s^2} \right)^{-5/2}, \quad (10)$$

with total mass $M = 10^{11} M_\odot$ and with a scale radius of $r_s = 3$ kpc. The SMBH is set initially on a circular orbit at $r = r_{\text{vir}} = 16r_s/3\pi$.

The Plummer density profile was chosen for this test as the expected decay rate of the orbit can be derived analytically, and is given by Rodriguez et al. (2018) as (see also Binney & Tremaine 2008)

$$\frac{dr}{dt} = -\frac{8\pi G^2 \ln \Lambda \rho(r) \chi M_\bullet r}{V_c^3 [1 + 3(1 + r^2/r_s^2)^{-1}]}. \quad (11)$$

Here

$$V_c = \left(\frac{GM}{r} \right)^{1/2} \left(1 + \frac{r_s^2}{r^2} \right)^{-3/4} \quad (12)$$

is the circular orbit velocity, and

$$\chi = \text{erf}(X) - 2\pi^{-1/2} X \exp(-X^2), \quad (13)$$

where

$$X = \frac{V_c}{\sqrt{2}\sigma} \quad (14)$$

and σ is finally the velocity dispersion given by

$$\sigma = \sqrt{\frac{GM}{6\sqrt{r^2 + r_s^2}}}. \quad (15)$$

For the Coulomb logarithm we use the value (e.g. Binney & Tremaine 2008)

$$\ln \Lambda = \ln \left(\frac{b_{\text{max}}}{b_{90}} \right) = \ln \left(\frac{2r_{\text{vir}}}{Gm\sigma(r_{\text{vir}})^{-2}} \right) \approx \ln \left(\frac{10 \text{ kpc}}{35 \text{ pc}} \right) \approx 5.7, \quad (16)$$

where b_{max} and b_{90} are the maximal and 90 degree deflection impact parameters.

We run two KETJU simulations of this system at stellar particle counts of $N = 10^5$ and $N = 10^7$, or stellar particle masses of $10^6 M_\odot$ and $10^4 M_\odot$, resulting in SMBH to stellar particle mass ratios of 100 and 10^4 , respectively. These resolutions are representative of the range of resolutions that have been typically used in simulations of SMBH dynamics within galaxies. For the $N = 10^7$ particle run we use a softening length of $\epsilon = 50$ pc for interactions between stellar particles and a regularised region radius of $r_{\text{region}} = 3\epsilon = 150$ pc, while for the $N = 10^5$ particle run we use a softening length of $\epsilon = 100$ pc and a regularised region radius of $r_{\text{region}} = 3\epsilon = 300$ pc.

We also run the same runs with standard GADGET-4 to allow for a comparison of its behaviour to KETJU. For these comparison runs we also include a version of the $N = 10^7$ particle system using a small softening length of $\epsilon = 5$ pc, to show how using KETJU compares to simply increasing the resolution in standard GADGET-4. In the GADGET-4 runs the interactions between stellar particles and the SMBH are softened with the same softening length as the interactions between stellar particles, while in the KETJU runs the SMBH always uses non-softened gravity.

The results are shown in Figure 3. Both KETJU runs follow the analytic prediction very well until around $r = 1$ kpc, apart from some oscillations due to deviations from a circular orbit particularly at lower particle mass resolutions. The deviation from the analytic prediction at small radii is expected due to the assumptions of the analytic model breaking down, and is seen also in tests of other codes using this setup (e.g. Rodriguez et al. 2018; Mukherjee et al. 2021). Apart from the oscillations which are made more significant due to the increased stochasticity at lower particle counts, the dynamical friction captured by KETJU does not appear to depend on the resolution at these particle counts. There is also no apparent dependency on the softening length, as expected since the interactions with the SMBH are non-softened.

The standard GADGET-4 results on the other hand clearly deviate from the analytic prediction, with the deviation being stronger for larger softening lengths. This is expected, as the softened gravity for the SMBH prevents capturing close interactions with stellar particles and thus reduces the strength of the frictional force. The $\epsilon = 5$ pc softening length run produces results that are in reasonably good agreement with the analytic and KETJU results, but the simulation took about twice as long to complete as the $\epsilon = 50$ pc softening length KETJU run.

We also use this test setup to study the conservation of energy in the system. The relative error in the total energy of the system for the runs is shown in Figure 4. The total energy of the system decreases slightly with a final relative error of about 10^{-4} in both the standard GADGET-4 as well as the KETJU runs, but the energy conservation is still somewhat better when the system is run with KETJU. The relatively small effect of KETJU on the total energy conservation is expected, as only a small fraction of the stars have strong interactions with the SMBH where the more accurate integration in KETJU improves the energy conservation. The momentum conservation of the simulation is not measurably affected by KETJU in this test.

The test presented here used only stellar particles, but the results apply equally well to interaction with DM particles at the same mass resolutions, as the regularised integrator can be set to treat them in the same way as stellar particles. However, including DM in the regularised regions generally requires that it uses a similar mass resolution and the same softening length as the stellar particles. This is because too massive particles would compromise the SMBH dynamics, and due to the issue discussed in Section 3.5 interactions between the non-SMBH particles usually need to be softened, with the current version of the regularised integrator only supporting a single softening length.

Using such a high resolution for DM is often not feasible due to the large number of required DM particles. In those cases KETJU would only resolve the dynamical friction from stellar particles, while the interaction with DM would be integrated with the standard GADGET-4 integrator, causing it to be underestimated. For typical simulations this is likely not a significant problem, as the DM fractions in the centres of galaxies where the SMBHs are typically found are rather low (e.g. Cappellari et al. 2013), and most of the dynamical friction comes from the stellar particles. However, it might also be possible to pair KETJU with some alternative scheme for treating the unresolved dynamical friction from DM (e.g. Tremmel et al. 2015; Pfister et al. 2019; Ma et al. 2023) to improve the accuracy in these cases. In hydrodynamical simulations, the approach used in KETJU naturally cannot help in resolving the dynamical friction from gas (Ostriker 1999), and alternative approaches would need to be developed in addition.

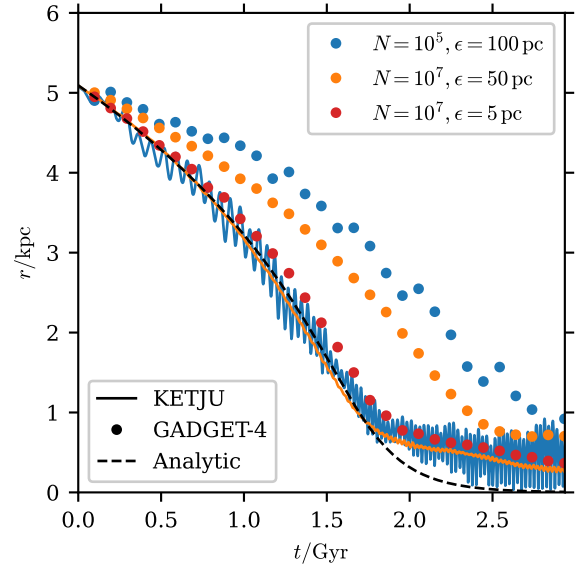


Figure 3. Sinking of an SMBH in a Plummer sphere of stellar particles due to dynamical friction. Simulations are run using different stellar particle counts N and gravitational softening lengths ϵ , using both KETJU and standard GADGET-4. The results are compared to an analytic prediction, which agrees well with the KETJU results as well as the GADGET-4 run with $\epsilon = 5$ pc.

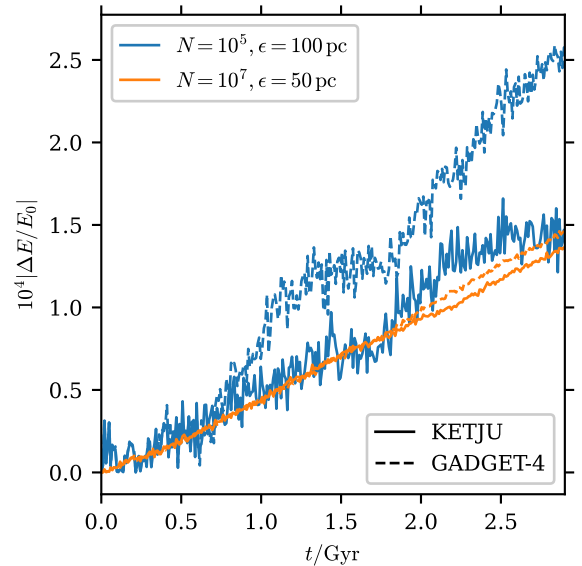


Figure 4. Relative error in the total energy of the same simulated systems as in Figure 3. The total energy is conserved on the level of $\sim 10^{-4}$ for both KETJU and standard GADGET-4, with the energy conservation being marginally better in the KETJU runs.

3.3 SMBH binary hardening rate

While the particle mass resolution does not significantly affect how well dynamical friction is resolved, it is well known from previous studies that this can have an effect on the hardening rate of SMBH binaries, with the hardening rate converging only at high enough mass resolutions (e.g. Berczik et al. 2006; Khan et al. 2011; Gualandris et al. 2017). To investigate the convergence of the SMBH binary hardening rate in KETJU simulations, we run a series of idealised, isolated galaxy mergers without gas.

Table 1. Resolution parameters of the galaxy models used in determining the binary hardening convergence. The subscripts \star and DM denote stellar and DM particle properties, respectively, with m being the individual particle mass, N the total number of particles, ϵ the softening length. M_\bullet is the mass of the central SMBH, and the final column gives the resolution of the simulation as defined by the logarithmic mass ratio between the SMBH and stellar particles.

$m_\star/(10^5 M_\odot)$	$\log_{10}(N_\star)$	ϵ_\star/pc	$m_{\text{DM}}/(10^7 M_\odot)$	$\log_{10}(N_{\text{DM}})$	$\epsilon_{\text{DM}}/\text{pc}$	$\log_{10}(M_\bullet/m_\star)$
0.5	6.70	5.0	1.0	6.66	300.0	4.8
1.0	6.40	5.0	2.0	6.36	300.0	4.5
2.0	6.10	5.0	4.0	6.05	300.0	4.2
5.0	5.70	5.0	10.0	5.65	300.0	3.8
10.0	5.40	10.0	20.0	5.36	600.0	3.5
20.0	5.10	10.0	40.0	5.04	600.0	3.2
50.0	4.70	10.0	100.0	4.60	600.0	2.8
100.0	4.40	20.0	200.0	4.30	1000.0	2.5

Each galaxy is modelled as a multicomponent sphere consisting of a $M_\star = 2.5 \times 10^{11} M_\odot$ stellar bulge, a $M_{\text{DM}} = 4.9 \times 10^{13} M_\odot$ DM halo, as determined by the $z = 0$ scaling relation of [Behroozi et al. \(2019\)](#), and a single SMBH of $M_\bullet = 3.0 \times 10^9 M_\odot$, which is consistent with observations (e.g. [Sahu et al. 2019](#)). Both the stellar and DM mass distributions follow a Hernquist profile

$$\rho(r) = \frac{Mr_s}{2\pi r(r+r_s)^3} \quad (17)$$

with scale radii $r_{s,\star} = 3.0 \text{ kpc}$ and $r_{s,\text{DM}} = 300 \text{ kpc}$, respectively.

To create the merging system, a pair of these galaxies is set on a near-radial (eccentricity $e \sim 0.99$) Keplerian orbit with an initial separation of $r_{\text{sep}} \sim 20 \text{ kpc}$ and first pericentre passage distance of $r_{\text{peri}} \sim 8 \text{ kpc}$. We run mergers using eight different mass resolutions M_\bullet/m_\star , provided in [Table 1](#). We create four realisations of the galaxy model per mass resolution, using different pseudo-random number generator seeds when sampling the particle phase space distribution. We then merge each combination of the model galaxy realisations at a given mass resolution, resulting in ten unique mergers per mass resolution. The runs with different mass resolutions use different stellar and DM particle softening lengths, chosen so that the number of stellar particles within the regularised region radius, $r_{\text{region}} = 3\epsilon_\star$, does not grow larger than a few thousand in order to keep the computational cost at a reasonable level. Each merger simulation is run for 500 Myr, which is long enough for the SMBH binary to shrink to a parsec-scale separation.

To quantify the binary hardening rate, we compute the inverse semimajor axis $1/a$ and the corresponding hardening constant H ([Quinlan 1996](#)):

$$\frac{d}{dt} \left(\frac{1}{a} \right) = H \frac{G\rho}{\sigma}, \quad (18)$$

where a is the binary semimajor axis, ρ is the stellar density and σ is the stellar velocity dispersion within the influence radius r_h of the binary. The influence radius is defined so that the enclosed stellar mass $M_\star(r_h)$ satisfies $M_\star(r_h) = 2M_{\text{binary}}$. To determine the value of H , we fit a linear function to $1/a$ in the range between the hardening radius $a = a_h = r_h/16$ (e.g. [Merritt 2013](#)) and $a = 10 \text{ pc}$, which occurs before GW emission becomes the primary hardening mechanism of the binary. For each simulation, we use the median value of ρ/σ determined from the set of snapshots after $a = a_h$. This ensures that our method is not sensitive to fluctuations in σ at early times when the merger remnant has not yet reached an equilibrium.

The convergence of the hardening parameter H with increasing mass resolution can be easily seen from [Figure 5](#), with the mean value of the set of runs at each resolution being nearly constant at high mass resolutions. To more rigorously quantify the convergence of the

hardening rate, we use a statistical test to see when the distributions of H from the sets of runs at different resolutions have become indistinguishable from each other. We thus wish to investigate the following test hypothesis:

$$\begin{cases} H_{\text{null}} : & \text{the variance between two sets is indistinguishable} \\ H_{\text{alt}} : & \text{the variance between two sets is not indistinguishable} \end{cases}$$

To do this, we perform a permutation test for each pair combination (A, B) of mass resolutions. The test is detailed in [Efron & Tibshirani \(1993\)](#), with the main steps briefly outlined here. We collect the observations from set A and the observations from set B into a single vector V of length N_T , where N_T is equal to the sum of the lengths of A and B , $N_T = N_A + N_B$. We determine the variance of the first N_A elements in V , labelling this as σ_A^2 , and the variance of the final N_B elements in V , labelling this as σ_B^2 . As a test statistic, we calculate the logarithm of the ratio of these two variances, namely:

$$t_{\text{stat}} = \log_{10} \left(\frac{\sigma_A^2}{\sigma_B^2} \right). \quad (19)$$

The test statistic is $t_{\text{stat}} = 0$ if the variances of the two samples are indistinguishable, i.e. when $\sigma_A^2 = \sigma_B^2$. We build a distribution of this test statistic by shuffling the elements in V without replacement $N_{\text{reps}} = 10^4$ times, generating a series of test statistics $t_{\text{stat},i}$. For each permutation of V , we determine the variance in the first N_A elements, and the variance in the final N_B elements, and calculate t_{stat} . This allows us to assess how likely the original value of t_{stat} is against random realisations of the values in sets A and B . To calculate the probability of observing the original value of t_{stat} under the null hypothesis, we use the two-tailed p -value:

$$p = \frac{2}{N_{\text{reps}}} \min \left(\sum_i [t_{\text{stat},i} < t_{\text{stat}}], \sum_i [t_{\text{stat},i} > t_{\text{stat}}] \right), \quad (20)$$

where $[q] = 1$ if q is true and 0 otherwise, and the min-function is used as we do not assume symmetry of the distribution of $t_{\text{stat},i}$ about some location parameter (e.g. the mean in the case of a normal distribution). We must then decide to what level of confidence α we will either reject or accept the null hypothesis. We follow established convention and choose $\alpha = 0.001$, i.e. the 99.9% confidence interval. Following the standard procedure of hypothesis testing, if $p < \alpha$, then we reject the null hypothesis in favour of the alternate hypothesis: the variance in hardening rate in set A is not indistinguishable from the variance in the hardening rate in set B to the confidence level given by α . Conversely, if $p > \alpha$, then we cannot reject the null hypothesis, and thus must instead accept the null hypothesis.

In [Figure 5](#) we show the mean and standard deviation of H for

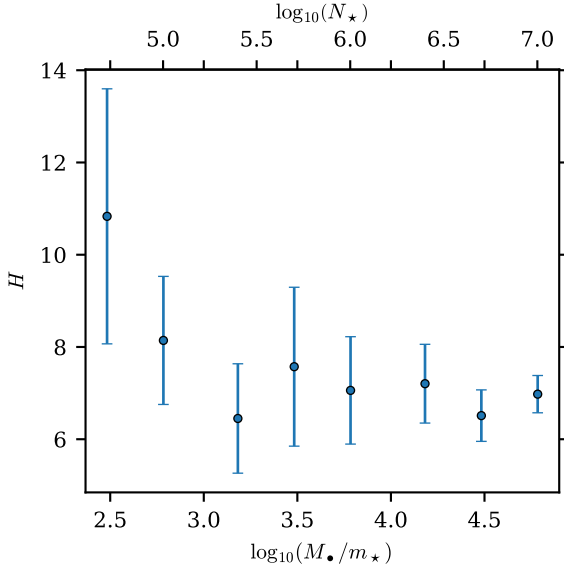


Figure 5. The mean and standard deviation of the hardening parameter H as a function of mass resolution. The spread in the data decreases with increasing mass resolution.

each mass resolution, while Figure 6 shows the p -value from the permutation test. The p -value for each combination of sets A and B is shown in the respective cell in Figure 6, and as indicated in the figure a mass resolution of $\log_{10}(M_*/m_*) \gtrsim 3.0$ is required for the variance between mass resolution samples to become consistently indistinguishable, and thus satisfy our convergence criterion. By consistently indistinguishable, we mean that for a set A , every set B of higher mass resolution has a p -value less than the significance level α . Some lower resolution samples (e.g. $\log_{10}(M_*/m_*) \sim 2.5$) also satisfy the convergence criterion when compared to other low resolution samples (e.g. $\log_{10}(M_*/m_*) \sim 3.5$), but fail to satisfy the criterion when compared to higher resolution samples (e.g. $\log_{10}(M_*/m_*) \sim 4.5$): thus at this mass resolution, consistent convergence is not achieved.

In order to better understand the hardening convergence for different mass resolutions, it is informative to investigate the number of stellar particles that are able to interact with the SMBH binary: namely, those stellar particles that reside within the loss cone of the SMBH binary. A particle in the loss cone has a specific angular momentum J that satisfies:

$$J < J_{lc} = \sqrt{2GM_{bin}\mathcal{K}a}, \quad (21)$$

where \mathcal{K} is a dimensionless constant of order unity. We set $\mathcal{K} = 1$ following Gualandris et al. (2017).

Although the SMBH binary is expected to remain nearly stationary at the centre of the galaxy in the real Universe, at mass resolutions that can be used in simulations the individual interactions with stellar particles are strong enough to cause the binary to undergo Brownian motion around the centre (e.g. Bortolas et al. 2016). This motion affects the number of stellar particles within the binary loss cone. To study how the random motion of the binary affects the number of particles in the loss cone, we calculate for each simulation snapshot the number of particles in the loss cone with respect to the actual position and velocity of the binary, and in addition with respect to ten additional possible positions and velocities where the binary could equally well have been located due to the Brownian motion. These additional positions and velocities are uniformly sampled on spheres around the stellar CoM, located using the shrinking sphere method

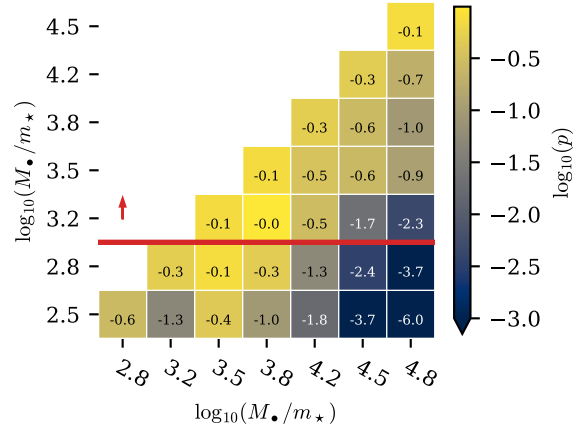


Figure 6. Two sample permutation test of the ratio of variances between samples. Points are coloured by the permutation test p -value. A mass resolution $\log_{10}(M_*/m_*) \gtrsim 3.0$, marked with the red horizontal line, is required for consistent convergence.

(Power et al. 2003), with radii corresponding to the actual distance and relative velocity of the binary to the stellar CoM.

The median number of stellar particles within the binary loss cone across the sampled possible binary positions, and the corresponding median stellar mass are shown in the top two panels of Figure 7 for each of the tested mass resolutions as a function of time since the SMBHs formed a bound binary system. We use the interquartile range (IQR) as a measure of the spread of the number of stars in the binary loss cone at each time bin, as shown in the bottom panel of Figure 7. We find that the stellar mass within the loss cone is consistent between mass resolutions, with higher mass resolution simulations ($\log_{10}(M_*/m_*) \gtrsim 4.0$) displaying less scatter as compared to lower mass resolution simulations ($\log_{10}(M_*/m_*) \lesssim 3.0$), as well as displaying less overall sensitivity to the Brownian motion of the binary. This resolution dependence is visible as the vertical colour gradient in the bottom panel of Figure 7.

Critically, we find that there are prolonged periods where very few stellar particles reside within the SMBH binary loss cone for low mass resolution simulations, whereas the loss cone is never depleted for high mass resolution systems. An emptied loss cone corresponds to an absence of stellar particles that are able to undergo hard scattering interactions with the SMBH binary, thus stalling the hardening of the binary. Indeed, having only a few stellar particles within the loss cone dramatically decreases the efficiency with which the binary can impart orbital energy and angular momentum to the stellar particles, introducing large stochasticity in the rate at which the binary hardens. Ultimately, this stochasticity in hardening rate manifests itself as the scatter observed in Figure 5 for low mass resolutions. With an increased particle count, the higher mass resolution simulations have a steadier flow of particles that are able to harden the SMBH binary than their low resolution counterparts, resulting in reduced scatter in the hardening rate H .

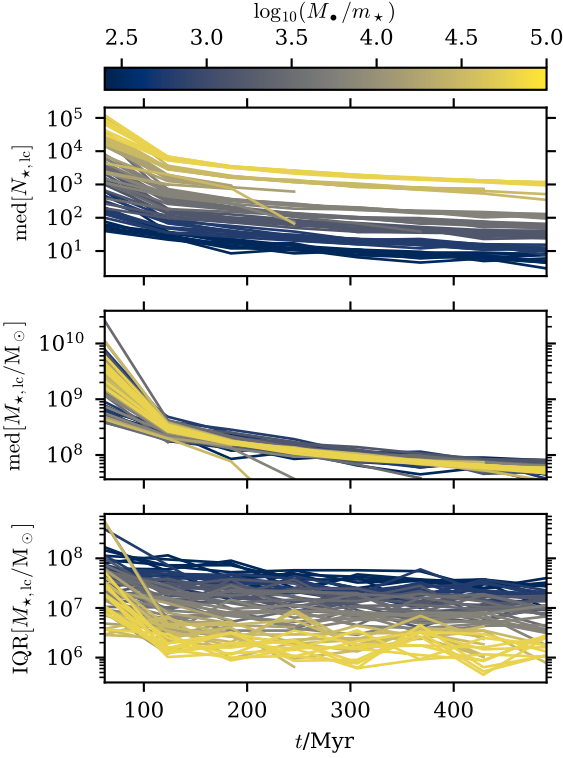


Figure 7. *Top:* Number of stellar particles within the loss cone as a function of time since the SMBH binary forms a bound system. The number of particles inside the loss cone dramatically decreases with decreasing mass resolution. As a result of poor mass resolution, there are prolonged periods of an almost-empty loss cone, effectively stalling the SMBH binary hardening. *Middle:* Median stellar mass within the loss cone for the same time period as the top panel for each simulation, sampled over ten possible binary phase-space locations. *Bottom:* The interquartile range (IQR) of stellar mass within the loss cone for the same time period as the top panel for each simulation. The IQR is determined using the same sampling method as for the median in the middle panel. Whilst the median stellar mass within the loss cone is consistent between mass resolutions, the scatter shows a gradient of higher mass resolutions corresponding to a reduced scatter. In other words, the mass entering and exiting the loss cone varies more smoothly with increased mass resolution, as expected.

3.4 Loss cone refilling in a spherical system

To supplement the hardening rate convergence test in realistic systems presented in the previous section, we perform here in addition an idealised test to check how accurately the large-scale gravitational dynamics of GADGET-4 capture the processes that refill the loss cone. We repeat the test of Gualandris et al. (2017) for loss cone refilling in an isolated Hernquist sphere, where loss-cone refilling mainly occurs due to two-body relaxation. This makes the refilling rate sensitive to the accuracy of the gravitational interactions far from the centre of the galaxy. Critically, Gualandris et al. noted that in this test GADGET-2 did not produce converged results with the expected $R_J \propto N^{-1/2}$ scaling observed with other codes, where N is the number of stellar particles. The authors attributed this to individual random large force errors caused by the gravity algorithms adopted in GADGET-2, and here we wish to confirm whether such errors are also present in GADGET-4.

The test setup consists of a single Hernquist stellar sphere, which we set to have a mass of $M = 10^{10} M_\odot$ and a scale radius of $r_s = 1$ kpc. We however note that the system can always be scaled to a

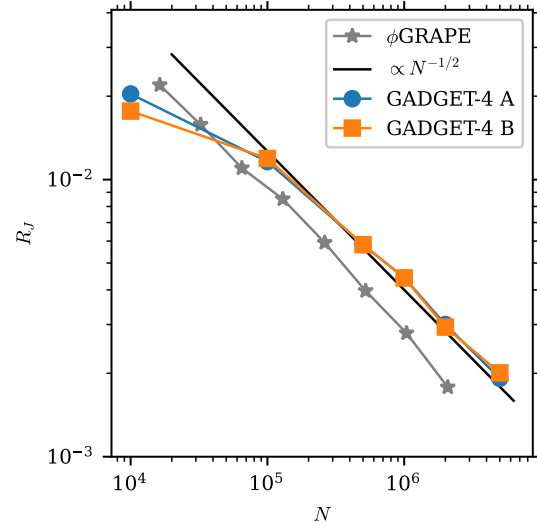


Figure 8. The loss cone refilling parameter R_J in an isolated Hernquist sphere as a function of different particle counts N using different GADGET-4 configurations (see the text for details). In addition to the GADGET-4 results, the figure also shows the results for the same test system using the ϕ GRAPE-code, extracted from figure A1 of Gualandris et al. (2017), as well as the expected $R_J \propto N^{-1/2}$ scaling.

dimensionless unit system with $M = r_s = G = 1$, so that the specific parameter values are not important here. Following Gualandris et al. (2017), the softening length is set to

$$\epsilon = \left(\frac{2\pi}{N} \right)^{1/3} \text{ kpc}, \quad (22)$$

although in GADGET-4 this results in slightly less softened interactions compared to the Gualandris et al. simulations which use Plummer-softening. The system is then evolved for approximately 1 Gyr using different combinations of code options. We store 50 snapshots during the evolution, and evaluate from these snapshots the refilling parameter

$$R_J = \frac{N_J}{N}, \quad (23)$$

where N_J is the total number of unique stellar particles that enter the loss cone during the simulation, i.e. have their angular momentum reduced to $J < J_{lc}$. To evaluate the angular momentum with respect to the galactic centre, we find the location of the centre using the shrinking spheres method for each snapshot. For the loss cone angular momentum we use the value of $J_{lc} = 0.005 \sqrt{GM r_s}$, thus matching figure A1 of Gualandris et al. (2017).

In Figure 8 we show the results of this test with different GADGET-4 code configurations, compared against the results of Gualandris et al. (2017). Configuration A is the same as is used for most other runs presented in this paper, i.e. using FMM with second order multipoles, hierarchical time integration, and force and integration error tolerances set to $\alpha = 0.005$ and $\eta = 0.002$, respectively. Configuration B uses the same tolerances, but uses instead the one-sided tree calculation of gravity with first order multipoles together with the traditional nested time integration scheme, mimicking thus the configuration used by the GADGET-3 version of KETJU that has been used in previous KETJU studies.

Both configurations display nearly identical results, following the expected $R_J \propto N^{-1/2}$ scaling observed by Gualandris et al. (2017), except at the very lowest resolutions. The R_J -values are however

slightly larger than those obtained by [Gualandris et al.](#) using the ϕ GRAPE-code for the same setup, which might be due to the different treatment of the gravitational softening. In any case, we see no evidence of the type of clearly erroneous behaviour that [Gualandris et al.](#) observed to occur when using GADGET-2. The loss cone refilling rate appears to be correctly captured using our reference code configuration, and in addition the rate is not very sensitive to the specific code options.

We have also performed this analysis using different force and integration error tolerances, and found only slight differences when using reasonable tolerance parameters between the default values recommended for general GADGET-4 simulations and tolerances up to ten times smaller than the reference tolerances adopted here. In addition, performing this analysis for the merger runs of Section 3.3 showed that the refilling parameter is essentially independent of the system mass resolution, with this result again being consistent with the results of [Gualandris et al. \(2017\)](#).

3.5 Stellar softening in the regularised integrator

While the regularised integrator can integrate systems without requiring softening, when combined with a large-scale GADGET-4 simulation it is often necessary to include the same softening as used by GADGET-4 in the interactions between stellar particles also in the regularised integration. Otherwise a stellar particle moving in or out of a regularised region would experience a sudden jump in potential energy as its interaction with the other stellar particles in the region changes between softened and non-softened. The energy error from such jumps can be particularly significant when the region contains a relatively large mass of stellar particles compared to the central SMBH. Such energy errors can lead to the formation of artificial stellar cusps, while including stellar softening in the regularised integration avoids such spurious effects.

This effect is demonstrated in [Figure 9](#), which shows the number of particles within the regularised region during a 400 Myr simulation of a Hernquist sphere galaxy model with a stellar mass of $M_\star = 3 \times 10^{11} M_\odot$ resolved using two million particles, hosting a $M_\bullet = 3 \times 10^8 M_\odot$ SMBH at its centre. The stellar softening is set to $\epsilon = 30$ pc for this run, with a regularised region radius of $r_{\text{region}} = 90$ pc. Due to this large region radius, the region initially contains about 1300 stellar particles, corresponding to a total mass of about $2 \times 10^8 M_\odot$, which is comparable to the mass of the SMBH. The simulation is run both with and without stellar softening in the regularised integration. The run without softening shows a rapid increase in the central density due to the energy errors explained above, while the density in the run with softening remains approximately stable. Similar effects would also appear if the regularised region was allowed to be made smaller than the softening kernel, due to the interactions between the SMBH and stellar particles then also discontinuously transitioning between softened and non-softened forms. To avoid these issues, all the other runs in this paper use softening between stellar particles in the regularised regions.

For comparison, we also run simulations with a $\epsilon = 3$ pc softening, a $r_{\text{region}} = 9$ pc regularised region radius, and an SMBH with $M_\bullet = 3 \times 10^9 M_\odot$. These settings result in the region containing about $3 \times 10^6 M_\odot$ mass of stellar particles. In this case the effect of the energy errors appears insignificant, which is due to the SMBH completely dominating the gravitational dynamics within the regularised region. The difference in the region particle count between the runs is only ~ 2 – 3 particles, which is comparable to the random variation during the simulations, and could be caused purely by random variations

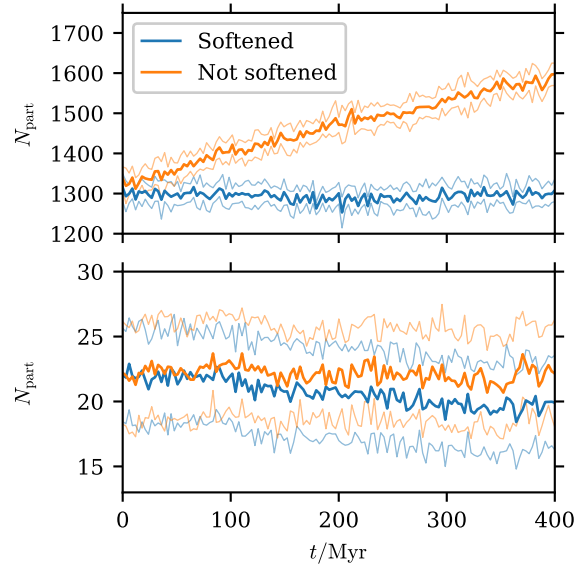


Figure 9. The evolution of the number of particles within the regularised region in simulations run with (blue lines) and without (orange lines) softening between stellar particles in the regularised integrator. Simulations are run with either $r_{\text{region}} = 90$ pc and $M_\bullet = 3 \times 10^8 M_\odot$ (top panel) or $r_{\text{region}} = 9$ pc and $M_\bullet = 3 \times 10^9 M_\odot$ (bottom panel). The data is smoothed over a small time window of 3 Myr to reduce the stochastic oscillation of the particle count, with the thick lines showing the mean and the thin lines showing the $\pm 1\sigma$ limits. When softening is not used, the density rapidly increases in the large region run in the top panel due to energy errors when particles enter and exit the region, leading to the formation of an artificial stellar cusp. In the small region run in the bottom panel this effect is not clearly apparent, as the SMBH dominates the dynamics within the region, and the energy errors in stellar interactions are thus insignificant.

between the runs. These runs resemble the configuration used in some earlier simulations run with KETJU (e.g. [Rantala et al. 2017, 2018](#)), and thus demonstrate that in such situations the error from not using softening within the regularised integrator is unimportant.

The approach of using the same softening for interactions between stellar particles in the regularised integrator as is used in the main GADGET-4 simulation is the simplest solution to avoiding energy errors when particles enter and exit the regularised region, but it has some potential issues for some applications. For instance, in very high-resolution simulations where the stellar particles have physically realistic masses, it might be desirable to integrate the regularised regions without any softening to capture relaxation processes in the stellar clusters around SMBHs. Depending on the softening length used on the GADGET-4 side and the other details of the system, the energy error in the transition to non-softened interactions might still be large enough to compromise the results of such a simulation. Thus, some other kind of scheme for smoothly transitioning between softened and non-softened interactions might be needed for such applications. The current implementation also prevents including multiple particle types with different softening lengths in the regularised regions, which might be desirable in some situations. However, for most applications of KETJU that we can foresee, the current approach of handling gravitational softening in the regularised regions should be satisfactory.

3.6 Integrator tolerance and PN corrections

When running simulations with the PN-corrections enabled, the integrator tolerance ϵ_{GBS} plays an important role in capturing the effects of the corrections on the binary orbit. To test the effects of the integrator tolerance on the evolution of a binary using the full 3.5PN equations of motion implemented in the code, we integrate an SMBH binary in isolation until merger using a range of integration tolerances.

The binary components have masses of $M_1 = 10^9 M_\odot$ and $M_2 = 5 \times 10^8 M_\odot$, and the initial orbit has a semimajor axis of $a = 200G(M_1 + M_2)/c^2 \approx 0.03$ pc and an eccentricity of $e = 0.1$. Starting from this initial condition it takes about 5.3×10^5 yr for the binary to merge due to GW emission, during which time it completes tens of thousands of orbits. The output time relative tolerance was fixed to $\epsilon_t = 10^{-10}$ for these runs to ensure that differences in the times of the output points do not introduce significant additional errors.

The resulting relative errors in various orbital parameters compared to a reference run using a tolerance of $\epsilon_{\text{GBS}} = 10^{-12}$ are shown in Figure 10. In addition, we show in Figure 11 the relative error in the time of the binary ‘merger’ based on the merger condition defined in Eq. (3). Larger tolerance values result in relatively large errors, however the errors converge well with smaller tolerance values, so that tolerances below $\epsilon_{\text{GBS}} \lesssim 10^{-7}$ match the reference solution to sub-percent level over the entire integration period.

However, following the orbital phase to within one full orbit requires a relatively high tolerance of $\epsilon_{\text{GBS}} \lesssim 10^{-9}$. For longer integrations the errors accumulate to larger total values, but since in typical simulations the effects of the surrounding stellar environment are significant and have inherent inaccuracy due to the unphysically large particle masses, tolerances of $\epsilon_{\text{GBS}} = 10^{-9}$ – 10^{-7} should provide the right balance between capturing the SMBH binary orbital dynamics and the computational cost for most applications.

3.7 Computational scaling

The scalability of both the regularised MSTAR integrator (Rantala et al. 2020) and the GADGET-4 code (Springel et al. 2021) have been studied extensively in isolation. How the combined KETJU code scales depends mainly on the relative computational cost of the regularised integration compared to the rest of the system, which depends on both the number of particles in the system and the details of the particular simulation setup, which together determines how difficult the integration is to perform at the set tolerances. Here we restrict our study to investigating the strong scaling of the code, i.e. how quickly the same problem is solved when increasing the number of CPU cores. We test the computational scaling for two cases where the regularised integration is either the dominant contribution or only a small fraction of the total computational cost.

For the first test case, we run short simulations of an isolated spherical galaxy consisting of a $M_\star = 10^{11} M_\odot$ stellar component with a $\gamma = 1.5$ Dehnen density profile and an effective radius of $R_e = 5$ kpc set in a DM halo with a mass of $M_{\text{DM}} = 4 \times 10^{13} M_\odot$ following a $\gamma = 1$ Dehnen profile. Both the stellar and DM components are resolved using 10^7 particles. To create a system where the regularised integration is the dominant contribution, we place a BH binary with masses of $M_{\bullet,1} = 10^8 M_\odot$ and $M_{\bullet,2} = 3.33 \times 10^8 M_\odot$ on an orbit with a semimajor axis of $a = 3$ pc and an eccentricity of $e = 0.6$ in the centre of the galaxy. We further set the stellar softening length to $\epsilon = 7$ pc and $r_{\text{region}} = 21$ pc, yielding about 4000 particles in the region and thus making regularised integration computationally dominant over the softened dynamics integration in GADGET-4.

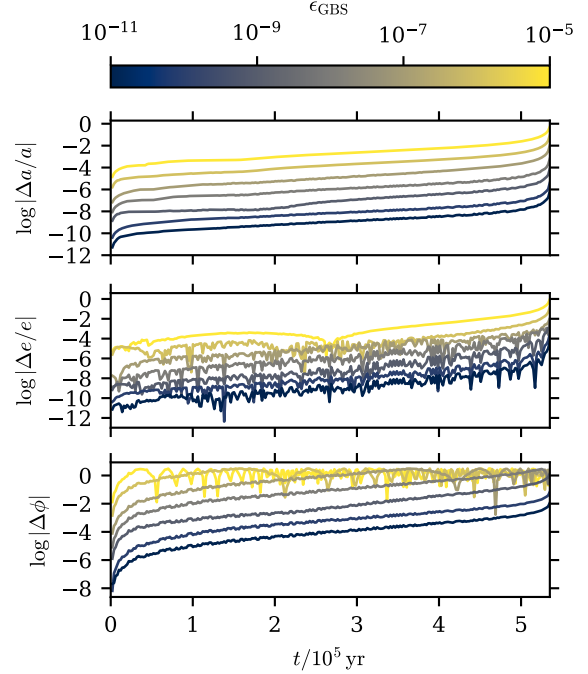


Figure 10. The relative error in the semimajor axis a (top panel), the eccentricity e (middle panel), and the error in the orbital phase ϕ (bottom panel) between runs of an isolated SMBH binary at different integrator tolerances ϵ_{GBS} . The errors are calculated with respect to a reference run using a very high accuracy of $\epsilon_{\text{GBS}} = 10^{-12}$.

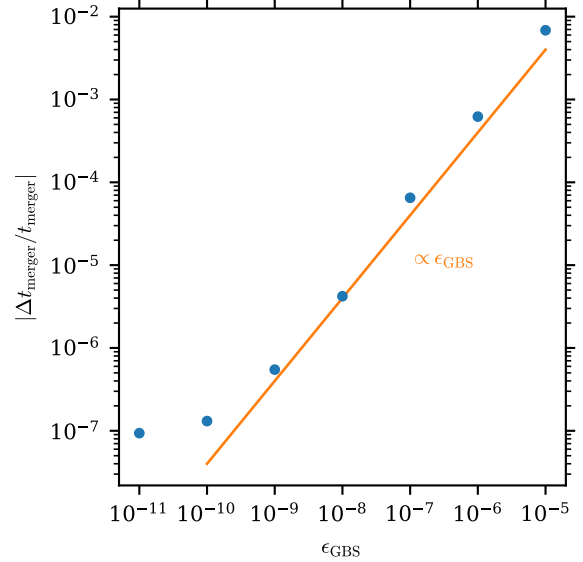


Figure 11. The relative error in the time when the SMBH binary system reaches the integrator merger condition, as defined in Eq. (3), compared to a reference run using $\epsilon_{\text{GBS}} = 10^{-12}$. The error appears to scale nearly linearly with the tolerance, but saturates at the smallest tolerances where the error is a fraction of an orbital period and is mainly due to the merger condition being only evaluated after each full integrator step.

Table 2. The stellar mass, effective radius R_e , and the scale radii r_s for the Hernquist sphere stellar and DM components of the individual initial galaxies in the runs with different numbers N_{gal} of galaxies.

N_{gal}	$M_{\star}/(10^{11} M_{\odot})$	R_e/kpc	$r_{s,\star}/\text{kpc}$	$r_{s,\text{DM}}/\text{kpc}$
2	2.00	4.79	2.65	233
3	1.33	3.76	2.08	182
5	0.80	2.77	1.53	134

For the second test case where the regularised integration is only a small fraction of the computational cost, we use a single BH of mass $M_{\bullet} = 10^8 M_{\odot}$ in the centre of the galaxy with a stellar softening length of $\epsilon = 2 \text{ pc}$ and a small regularised region radius of $r_{\text{region}} = 6 \text{ pc}$, yielding about 600 particles in the region. In typical applications, the main factor in deciding the size of the regularised region is the lower limit imposed by the chosen softening length. The softening lengths used here are chosen to match what would be typically adopted for the chosen region sizes, as the softening length affects the performance of the main GADGET-4 integration. We run these systems for 10^5 yr using varying numbers of CPU cores ranging from $N = 16$ to 1024.

The results of this strong scaling test are shown in Figure 12. The total time taken by the code can be seen to scale nearly ideally at low CPU counts in both systems, whereas at very high core counts in particular the single BH case begins to even slow down. For both cases the time taken in the GADGET-4 part is very similar, although slightly less wallclock time is spent for the binary BH system for which the softening length is somewhat larger. The scaling of the GADGET-4 part of the calculations stops at around a 100 CPUs for this system, corresponding to the size of a single node on the Mahti supercomputer.

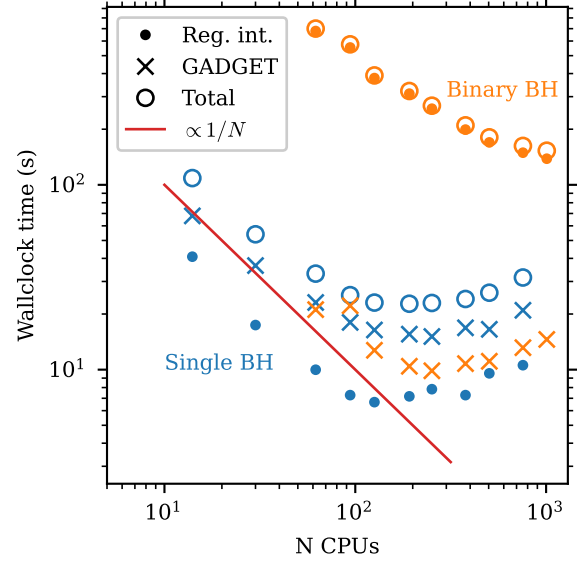
The scaling of the regularised integration also stops around the same point for the single BH system, so that for this system the code cannot make use of a larger number of CPUs. On the other hand, in the binary BH case the simulation time is dominated by the regularised integration, as the region is more computationally expensive due to both the larger particle count as well as the presence of the BH binary. The higher particle count allows the regularised integrator to scale nearly ideally to a much higher number of CPUs, allowing also the total run time to scale well despite the fact that the GADGET-4 part is also becoming slightly slower for larger CPU numbers in this system.

These results show how the scalability of the code depends on the relative cost of the regularised integration, and how in cases where the regularised integration is dominant the code can make use of much larger CPU counts than would be sensible for a standard GADGET-4 simulation of a system of the same size. These results are also in line with the extensive scaling test of the regularised integrator presented in Rantala et al. (2020), where it was found that the integrator scales well until $N_{\text{part}} \sim 10 N_{\text{CPU}}$. To avoid the slowing down of the integration at excessive core counts, the code automatically limits the number of CPUs allocated to each region based on its particle count.

4 FORMATION OF CORES IN MULTIPLE MERGERS

4.1 Simulations

As an example of the types of problems that can be studied with the public version of KETJU presented here, we perform a simplified study of how the number of progenitor galaxies affects the size of the

**Figure 12.** The strong scaling of the code in two different systems with a total of 10^7 stellar particles. In the first test case the regularised region contains ~ 4000 particles and an SMBH binary (orange symbols), while in the second test case the system includes only a single SMBH surrounded by a regularised region containing ~ 600 particles (blue symbols). The figure shows the wallclock times taken by the regularised integration (solid circles), the GADGET-4 part (cross symbols) and the combined total KETJU integration time (open circles), when the simulations are run using different numbers N of CPUs. The ideal scaling slope of $\propto 1/N$ is also indicated for reference.

core in the final merger remnant. The formation of cores in massive elliptical galaxies, which is commonly attributed to core scouring by SMBH binaries, has been already studied before using an earlier version of KETJU (Rantala et al. 2018), and also to a great extent by various other authors with different codes (e.g. Milosavljević & Merritt 2001; Milosavljević et al. 2002; Merritt 2006; Khan et al. 2012; Nasim et al. 2021; Dosopoulou et al. 2021).

Here the main difference to most other studies of this process is that multiple mergers are allowed to occur in quick succession without necessarily allowing each SMBH binary to merge first before the next galaxy merger. These simulations thus allow us to demonstrate how KETJU can be used to capture the complex dynamics in systems with multiple interacting SMBHs.

We simulate the mergers of three different systems with two, three, and five identical galaxies in the initial conditions, respectively. All systems are set to have the same total stellar mass of $M_{\star} = 4 \times 10^{11} M_{\odot}$, a total DM mass of $M_{\text{DM}} = 7 \times 10^{13} M_{\odot}$, and a total black hole mass of $M_{\bullet} = 2.5 \times 10^9 M_{\odot}$, with the total masses divided either between two, three or five galaxies, depending on the simulation.

The DM particles have a mass of $m_{\text{DM}} = 5 \times 10^6 M_{\odot}$ and a softening length of $\epsilon_{\text{DM}} = 100 \text{ pc}$, while the stellar particles have a mass of $m_{\star} = 10^5 M_{\odot}$ and a softening length of $\epsilon_{\star} = 15 \text{ pc}$. The BHs are surrounded by regularised regions with a radius of $r_{\text{region}} = 45 \text{ pc}$, with all BH-BH and BH-star interactions being non-softened. Only stellar particles are allowed to enter the regularised regions, while the DM acts as a smooth perturbing background on the dynamics and has softened interactions with all particles. With these parameters, the mass ratio between the initial SMBHs and stellar particles is $m_{\bullet}/m_{\star} \geq 5000$, and the final merged galaxy has about four million stellar particles, which should ensure converged behaviour of the SMBH binary hardening based on the tests presented in Section 3.3.

The initial galaxies are modelled as multicomponent Hernquist spheres, setup using Eddington’s formula (Binney & Tremaine 2008) and the methods described in Rantala et al. (2018). The projected stellar half-mass radii are set based on the galaxy stellar mass M_\star by

$$R_e = 3.16 \left(\frac{M_\star}{10^{11} M_\odot} \right)^{0.6} \text{ kpc}, \quad (24)$$

which approximately matches the observed size-stellar mass relation (Newman et al. 2012, table 1). The DM scale radius is then set so that the central DM fraction is $f_{\text{DM}} = 0.2$. The scale radii of the initial galaxies are listed in Table 2. Each galaxy is also given an SMBH at the centre, with initially zero spin for simplicity.

The galaxies are placed on initial orbits that result in rapid galaxy mergers, with relatively small initial separations compared to the sizes of their DM haloes. This is done in order to reduce the simulation time, and should not significantly affect the simulation outcome, as the stellar components of the galaxies do not overlap. The two-galaxy system is placed on a nearly parabolic orbit at an initial separation of 30 kpc, while the three-galaxy system has two galaxies on a similar orbit with an initial separation of 45 kpc with the third galaxy at rest at a distance of 35 kpc from the midpoint of these two galaxies. The five-galaxy system is initialised by generating random positions for the galaxies within a box with 80 kpc on a side, and then generating normally distributed velocities so that the system is in virial equilibrium, assuming that the galaxies are point masses.

To demonstrate the cosmological integration capabilities of KETJU, we place the two- and three-galaxy systems in the same periodic box with a $10 h^{-1} \text{ Mpc}$ comoving side length, ensuring that the separation of the systems is large enough not to interact with each other. We simulated this system starting from redshift $z = 1$ using a cosmology with $\Omega_m = 0.3$, $\Omega_\Lambda = 0.7$, and $h = H_0/100 \text{ km s}^{-1} \text{ Mpc}^{-1} = 0.7$. These choices do not meaningfully affect the dynamics of the merging systems, but simply serve to demonstrate that the code operates correctly also in a cosmological comoving setting. We run the five-galaxy system in standard non-comoving coordinates and non-periodic space. For the analysis of the results from both simulations we will use physical coordinates, and set time $t = 0$ at the start of the simulation. In order to study the effect of the SMBHs on the merger remnant structure, we also run versions of the simulations where the initial galaxy models are generated without central SMBHs.

For simplicity, we disable the GW recoil kicks during SMBH mergers. For the initial non-spinning SMBHs with equal masses such kicks would vanish in any case, but for the second- and third-generation mergers that are possible in the systems with multiple merging galaxies they might lead to the ejection of the final remnant SMBH from the galaxy (Mannerkoski et al. 2022). As the kick magnitudes sensitively depend on the SMBH spins and are effectively random, including them would add an unnecessary layer of complexity for interpreting the results of these simplified demonstration simulations. However, we note that the recoil kicks can significantly contribute to the formation of cores (Nasim et al. 2021), and they should thus be included in more comprehensive studies of the core formation mechanism.

4.2 SMBH dynamics

The behaviour of the SMBHs in the two-galaxy merger is relatively simple, as can be seen from the orbital parameters in Figure 13. The SMBHs form a binary on a moderate-eccentricity ($e \approx 0.7$) orbit in the centre of the merged galaxy after about 200 Myr. This binary

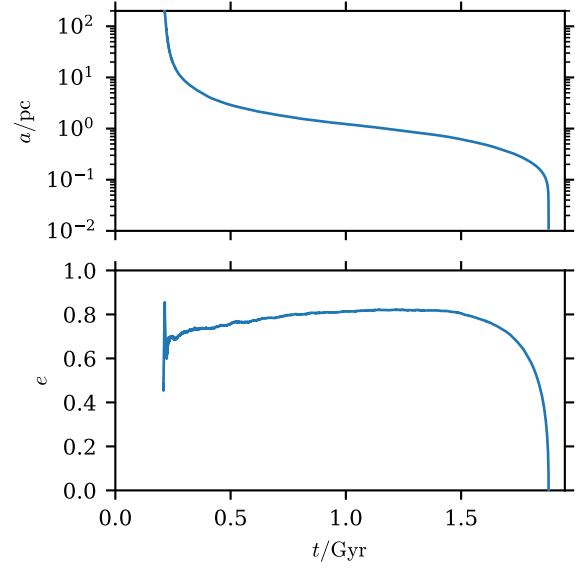


Figure 13. The semimajor axis a (top) and eccentricity e (bottom) of the SMBH binary formed in the two-galaxy merger. The initial binary eccentricity is $e \sim 0.7$ and the binary hardens due to stellar scattering with the final GW emission driven merger occurring ~ 1.5 Gyr after its formation.

then hardens due to stellar scattering and finally merges due to GW emission about 1.5 Gyr after it formed.

In the three-galaxy merger the behaviour is more complex, as can be expected since the chosen initial condition results in all three galaxies merging almost simultaneously. The orbital parameters of the bound binaries formed in this system are shown in Figure 14, with the SMBHs labelled A, B and C based on the internal simulation particle IDs and the SMBH binaries labelled with the corresponding letter pairs. Most of the time the system is in a hierarchical triplet state with a fairly wide outer orbit, but occasionally there are strong interactions between all three SMBHs when the outer orbit shrinks due to dynamical friction and stellar scattering. During these strong interactions the components of the central binary are sometimes exchanged, so that while A and B are the first SMBHs to form a bound binary, it is actually B and C that merge first due to GW emission. The time until the first SMBH merger from the formation of the first binary is slightly shorter here than in the two-galaxy merger, partly due to the strong interactions between the SMBHs contributing to the hardening of the inner binary. The remaining AB binary is left on a wide but highly eccentric orbit ($e \approx 0.98$), and it hardens efficiently enough to merge roughly ~ 1 Gyr later.

In the five-galaxy merger we label the SMBHs as A–E in order of their internal simulation particle IDs. After about 400 Myr, the galaxies hosting SMBHs C and D have merged, and the SMBHs form a bound binary. This binary quickly evolves to have an extremely high eccentricity ($e \approx 0.9995$) and then merges due to strong GW emission within only a few million years. The remnant SMBH is still labelled as C after this merger. The evolution of the orbital parameters of this binary is shown in Figure 15.

Over the next few hundred million years, the remaining galaxies merge together and the SMBHs begin interacting in the centre of the merged galaxy remnant. The evolution of the orbital parameters of the bound systems that are formed during these interactions is shown in Figure 16. First, after a period of complex interactions between all four remaining SMBHs in the system, SMBHs A and E form a binary on a high-eccentricity orbit ($e \approx 0.95$) and sub-parsec separation.

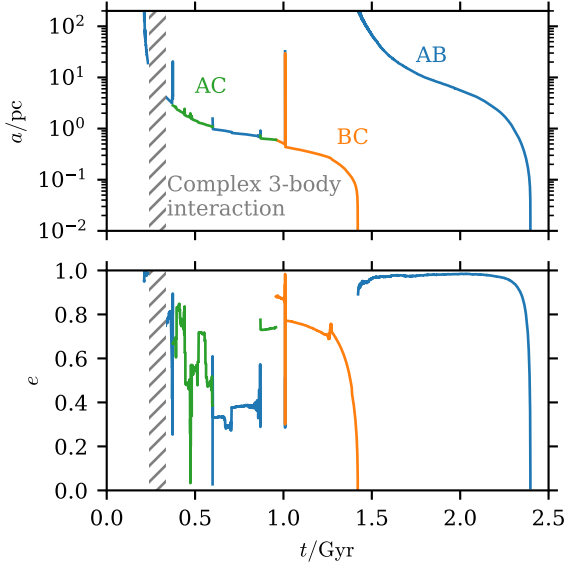


Figure 14. The semimajor axis a (top) and eccentricity e (bottom) of the SMBH binaries formed in the three-galaxy merger. In the hatched region the three SMBHs in the system have strong interactions with each other, and the orbital parameters cannot be meaningfully calculated. For most of its evolution, the SMBHs are in a hierarchical triplet configuration with a very wide outer orbit, with occasional close interactions that can change the component SMBHs in the inner binary, as shown in the figure. The outer orbit parameters are not shown for simplicity, as most of the time they are significantly affected by the stellar mass inside the very wide outer orbit.

This binary is already in the GW emission dominated regime of its orbital evolution and it is driven to merge within about 150 Myr.

Rapidly after this merger, SMBHs A and C form a wider binary, which interacts with SMBH B throwing it out to a wide orbit. These three SMBHs form a hierarchical triplet where the inner AC binary undergoes von Zeipel–Lidov–Kozai oscillations (Lidov 1962). As the orbit of SMBH B shrinks due to interactions with stars, it has several strong interactions with the central binary that throw it back out to a wide orbit, and finally ejects it completely from the galaxy. After this, the hardening of the AC-binary due to stellar scattering is quite weak. Based on analytical results for the stellar scattering driven hardening (Quinlan 1996) and GW emission (Peters 1964), we estimate that the binary would merge only at $t \sim 11$ Gyr. Running the simulation for this long would not bring enough additional benefit compared to the computational cost, and we therefore stop the simulation already at $t \approx 5$ Gyr.

4.3 Remnant density profiles and core sizes

The density profiles of the progenitor and merger remnant galaxies in the simulations are shown in Figure 17. The remnant profiles in the KETJU runs with SMBHs show clearly flattened central cores, with the size of the core increasing with the number of progenitor galaxies. In the runs without SMBHs the merger remnants retain the steepness of the progenitor density profiles also in the central parts (Boylan-Kolchin & Ma 2004). This shows that the presence of the SMBHs is responsible for the formation of these cores, in line with the findings of previous studies (e.g. Milosavljević & Merritt 2001; Merritt 2006; Rantala et al. 2018).

To quantify the size of the cores in the merger remnants, we fit

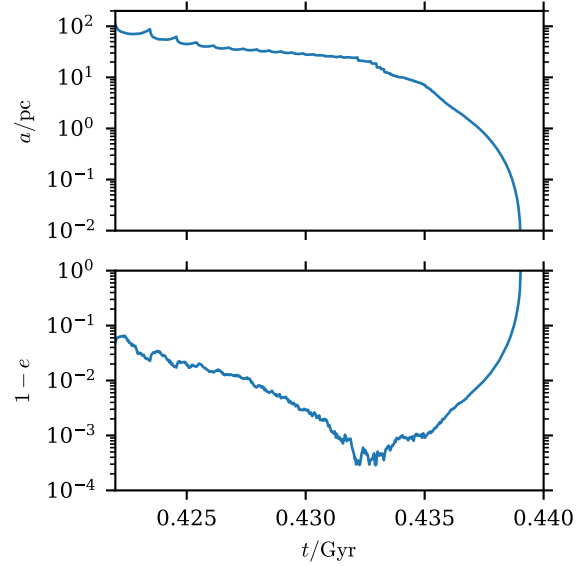


Figure 15. The semimajor axis a (top) and eccentricity e (bottom) of the binary formed by SMBHs C and D in the five-galaxy merger. The eccentricity is shown using $1 - e$ on a log-scale to make the extremely high eccentricity before the rapid GW-driven merger visible.

core-Sérsic profiles (Graham et al. 2003)

$$\Sigma(r) = \Sigma' \left[1 + \left(\frac{r_b}{r} \right)^\alpha \right]^{\gamma/\alpha} \exp \left[-b_n \left(\frac{r^\alpha + r_b^\alpha}{R_e^\alpha} \right)^{1/(an)} \right] \quad (25)$$

to the projected mass density profiles of the galaxies. Here n is the Sérsic index, R_e is the effective radius, r_b is the break radius, γ is the inner power law slope, α is a parameter controlling how sharp the transition between the power law and Sérsic profiles is, and $b_n \approx 1.9992n - 0.3271$. The fits were performed in the range $0.1 < r/\text{kpc} < 50$. The fitted parameters are shown in Table 3, and the corresponding profiles are shown in Figure 18.

The fitting results confirm what can also be seen visually from the density profiles: the size of the core, quantified by the break radius, increases for increasing numbers of progenitor galaxies, with the five-galaxy merger having a core that is almost twice as large as the core in the binary merger. The density profile within the core region also becomes flatter when the number of progenitors increases, and the overall size of the galaxy, as defined by the effective radius, also grows. These are both natural consequences of the stellar mass being displaced from the central regions due to interactions with the SMBHs.

The derived core size for our two-galaxy merger agrees well with the results of the binary merger of two Hernquist spheres ($\rho \propto r^{-1}$) with a similar final BH mass, obtained in Rantala et al. (2018). The fits also produce Sérsic indices of the merger remnants that are somewhat on the low-side, $2.4 \leq n \leq 3.2$, compared to $n \gtrsim 4$ typically observed for elliptical galaxies of similar masses. However, this is a well-known feature of the Hernquist model (Naab & Trujillo 2006) and also in good agreement with the findings of Rantala et al. (2018).

When comparing the simulated core sizes to observations, as defined by the observed M_\bullet – r_b relation (Thomas et al. 2016; Dullo et al. 2021), we find that the mean prediction is $r_b \sim 200$ pc for the SMBH mass in these systems, albeit with a rather large scatter. The core sizes are rather sensitive to the initial density profile of the galaxies, and as shown in Rantala et al. (2018) steeper density profiles ($\rho \propto r^{-1.5}$)

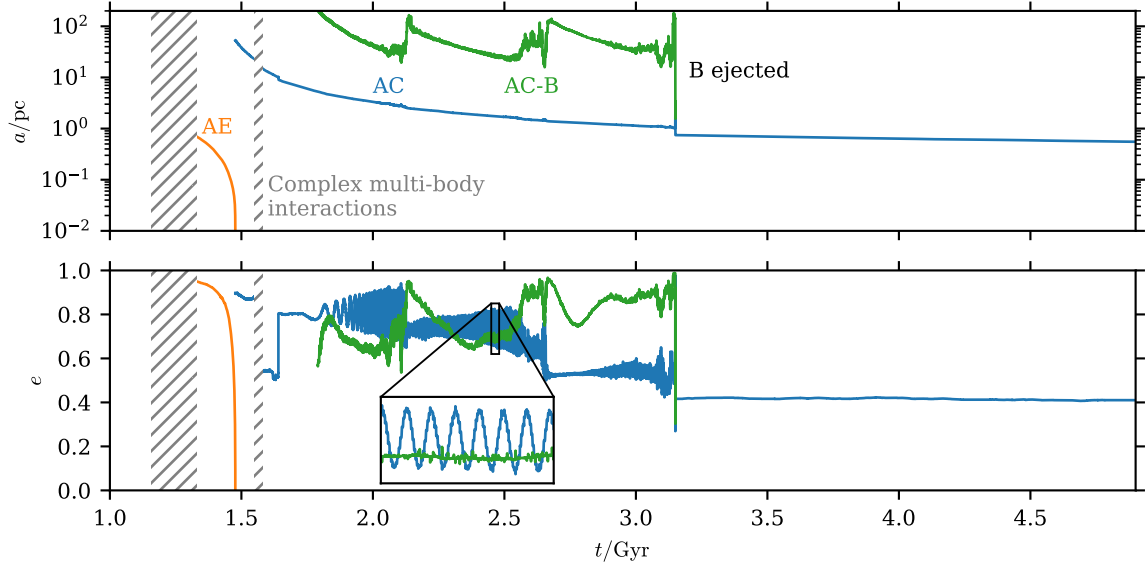


Figure 16. The semimajor axis a (top) and eccentricity e (bottom) of the SMBH binaries and hierarchical triplet that form after the CD binary has merged. In the hatched regions the multiple SMBHs in the system have strong interactions with each other, and the orbital parameters cannot be meaningfully calculated. The AC-B parameters show the orbit of SMBH B around the AC binary in a hierarchical triplet configuration. SMBH B has multiple close interactions with the binary that throw it onto a wider orbit, before finally being ejected completely from the galaxy. The inner AC binary also undergoes von Zeipel–Lidov–Kozai oscillations during this hierarchical triple phase.

Table 3. Core-Sérsic profile fit parameters and calculated mass deficits M_{def} for the merger remnant galaxies with different numbers N_{gal} of progenitors. The profile parameters are the break radius r_b , the effective radius R_e , the inner power law slope γ , the Sérsic index n , and the transition parameter α . Mass deficit results are shown for two different methods for calculating the mass deficit, see the text for details. Note that the final SMBH mass in the galaxy M_\bullet differs between the runs due to mass loss to GW emission and the ejection of an SMBH in the five-galaxy run.

N_{gal}	r_b/kpc	R_e/kpc	γ	n	α	$M_{\text{def},1}/10^9 M_\odot$	$M_{\text{def},1}/M_\bullet$	$M_{\text{def},2}/10^9 M_\odot$	$M_{\text{def},2}/M_\bullet$	$M_\bullet/10^9 M_\odot$
2	0.63	4.37	0.169	3.2	2.8	11.1	4.67	7.4	3.13	2.38
3	0.85	4.74	0.074	2.4	4.1	11.5	4.90	14.0	5.99	2.34
5	1.09	7.84	0.060	2.6	4.3	9.0	4.71	14.0	7.36	1.90

result in core sizes that are typically a factor of ~ 2 – 3 times smaller than the rather flat Hernquist profile. Steeper density profiles provide a better match to real observed elliptical galaxies, but are also more expensive to simulate, due to the higher central stellar density. Thus, as the main goal of this paper is to demonstrate the operation of the KETJU code in various simulation settings, we opted to run our simulations with the less steep Hernquist profiles.

4.4 Mass deficits

The size of the cores formed in mergers of galaxies with SMBHs can also be quantified in terms of the mass deficit, defined as the difference in stellar mass contained in the core region when compared to an equivalent galaxy without a core. The mass deficit is expected to scale with the total SMBH mass, with e.g. Merritt (2006) proposing a simple scaling based on the number of mergers N_{merger} ,

$$M_{\text{def}} \approx 0.5 N_{\text{merger}} M_\bullet, \quad (26)$$

whereas other studies have also found larger values, with the results depending to a significant degree also on the exact methods used to define the mass deficit (Dosopoulou et al. 2021). Observations show that the relative mass deficit is M_{def}/M_\bullet in the range 0.5–10 (e.g. Rusli et al. 2013).

To calculate this mass deficit for our runs, we use two different

approaches. In the first method we calculate the deficit ($M_{\text{def},1}$) based on the difference between the fitted core-Sérsic profile and a Sérsic profile fitted to the density profile outside the core region. In the second approach ($M_{\text{def},2}$), we use as a reference the equivalent galaxies and merger remnants from the corresponding runs without SMBHs, and calculate the difference in the mass contained within the region where the reference galaxy has a higher stellar density. The results of this calculation are listed in Table 3, and it can be seen that the two different approaches give reasonably similar results.

In all cases the ratio M_{def}/M_\bullet is larger than predicted by the relation (26), but consistent with the range of observed mass deficits (e.g. Rusli et al. 2013; Dullo et al. 2021). It is also interesting to note that using the second definition, the mass deficit is very similar in both the three- and five-galaxy mergers, and clearly larger than in the two-galaxy merger. The complex interactions in the multi-SMBH systems found in these systems might contribute to the relatively large mass deficits, as the repeated ejection of an SMBH to wide orbits within the galaxy could increase the effect it has on the stellar system. Kulkarni & Loeb (2012) also found similarly large mass deficits in systems with multiple interacting SMBHs. On the other hand, using the first definition for the mass deficit there does not appear to be any meaningful difference between the different mergers. As is the case with the core radii, the large mass deficit values are likely mainly due to the simplified Hernquist profile initial conditions, with e.g.

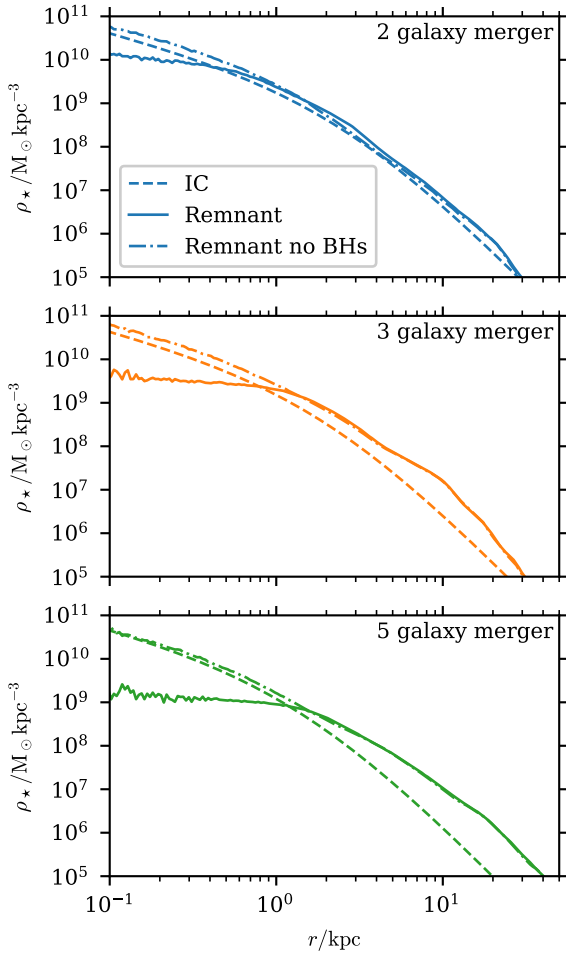


Figure 17. Stellar density profiles of the initial condition (IC) galaxy models, and the final merger remnants of the merging systems with different numbers of galaxies. In the simulations without BHs the initial density profile is retained, as expected.

Dosopoulou et al. (2021) finding a factor of ~ 3 larger mass deficits for $\rho \propto r^{-1}$ profiles compared to steeper initial density profiles with $\rho \propto r^{-1.5}$.

4.5 Velocity anisotropy profiles

The dynamical interaction between the SMBHs and the stellar particles is expected to lead to the preferential ejection of particles on radially biased orbits, and result in a tangential bias in the orbits of the stellar particles near the centre of the final merger remnant (Quinlan & Hernquist 1997; Milosavljević & Merritt 2001; Thomas et al. 2014).

This effect can be quantified using the velocity anisotropy parameter β , which is defined as (e.g. Binney & Tremaine 2008)

$$\beta = 1 - \frac{\sigma_\theta^2 + \sigma_\phi^2}{2\sigma_r^2}, \quad (27)$$

where σ_r , σ_θ , and σ_ϕ are the stellar velocity dispersions along the spherical coordinate directions. In Figure 19 we show the radial $\beta(r)$ -profiles of the merger remnants of the three runs, with two, three and five galaxy progenitors (top to bottom). The velocity anisotropy is computed in radial bins with logarithmic spacing around the centre of the final stellar component, and the shaded regions show the

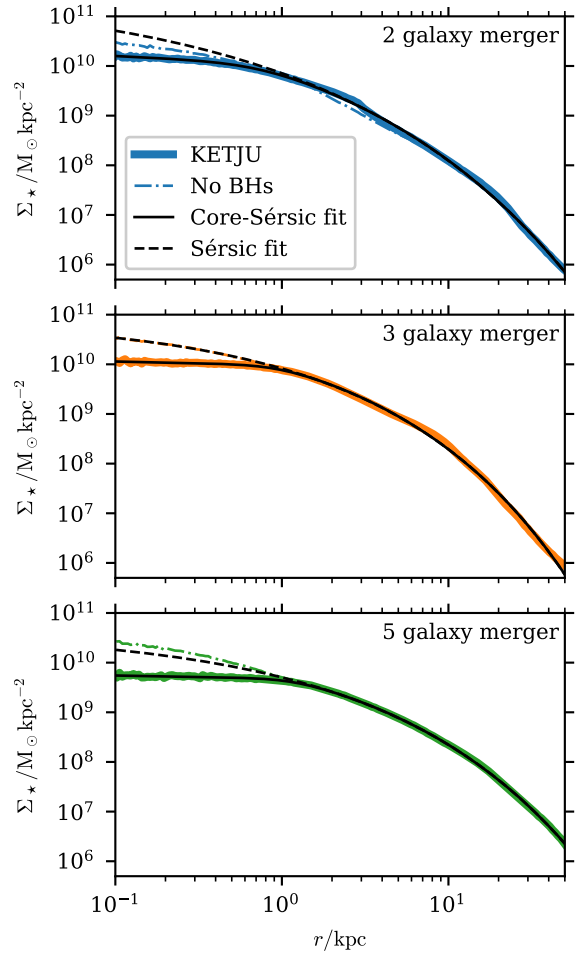


Figure 18. Projected stellar density profiles of the merger remnants as in Figure 17, the fitted core-Sérsic profiles, and the Sérsic profiles equivalent to the outer region of the core-Sérsic fits.

estimated 1σ -uncertainty due to the finite number of particles in each radial bin.

The profiles clearly show the expected behaviour of a slight tangential bias ($\beta(r) < 0$) in the centre that transitions to radial bias ($\beta(r) > 0$) in the outer parts of the galaxy, which is typical for collisionless mergers (Frigo et al. 2021). The effect of the SMBHs is also apparent when comparing the profiles of the runs with (solid lines) and without SMBHs (dash-dotted lines), as the runs without SMBHs show consistently larger values of $\beta(r)$. Finally, we note that the profile of the two-galaxy merger is also very similar to the profiles published by Rantala et al. (2018) for binary mergers with similar SMBH masses.

5 SUMMARY AND CONCLUSIONS

In this paper we have presented the new publicly available version of the KETJU code, as implemented in GADGET-4. We have demonstrated how the code can follow the dynamics of SMBHs to spatial scales significantly below the softening length used for stellar and other simulation particles, which is not possible with standard GADGET-4 or other similar softened N -body codes.

The presented code tests show that dynamical friction acting on SMBHs sinking in a stellar systems is captured well even at relatively

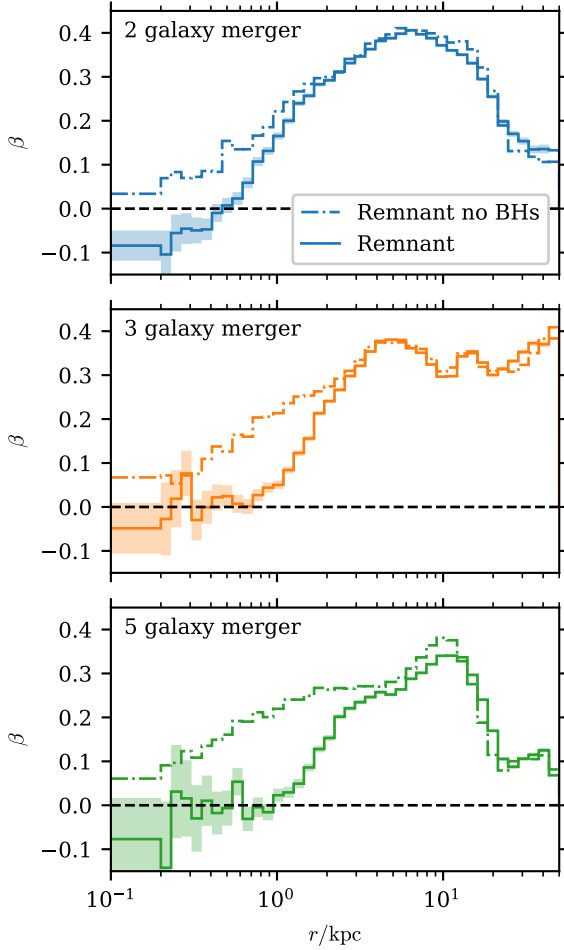


Figure 19. The stellar velocity anisotropy $\beta(r)$ profiles of the final merger remnants of the merging systems with different numbers of galaxies. The isotropic progenitor galaxies are shown as the black horizontal dashed line with $\beta(r) = 0$. The $\beta(r)$ profiles are computed in logarithmically spaced bins, with the shaded regions showing the estimated 1σ -uncertainty due to the finite number of particles in each radial bin. All profiles show the expected behaviour of an increasingly more tangentially biased velocity distribution at small radii due to the influence of the SMBH binary.

low particle resolutions. As all BH-BH and BH-star interactions are non-softened in KETJU, a comparable GADGET-4 run would have to be run with much smaller softening lengths and at a significantly higher computational expense (see Figure 3). We also show that the hardening rate of a SMBH binary due to stellar scattering converges when the mass ratio between the BH and stellar particles is $M_{\bullet}/m_{\star} \gtrsim 10^3$. For the applications presented here this corresponds to galaxy models with $\gtrsim 1$ million stellar particles. The convergence of the hardening rate can be explained by the reduced impact of the Brownian motion of the SMBH binary at higher mass resolutions, i.e. the stellar mass entering and exiting the loss cone varies more smoothly with increased mass resolution. The convergent behaviour of the hardening rate is similar to what has been previously found in studies using other high-accuracy N -body codes (Berczik et al. 2006; Khan et al. 2011; Gualandris et al. 2017). In line with this finding, we also confirmed that GADGET-4 does not suffer from the type of errors in modelling the loss cone refilling that have been previously reported for an earlier version of the GADGET code (Gualandris et al. 2017).

While the interactions between BHs and stars are always non-softened in KETJU, the star-star interactions can also be optionally softened even if the stars reside within the regularised region. Including this softening length will reduce energy errors as particles are moving in and out of the region and it is particularly important in simulations where a large stellar mass, comparable to the black hole mass, is contained within the regularised region.

The accuracy of the regularised MSTAR (Rantala et al. 2020) integrator, which uses a Gragg–Bulirsch–Stoer extrapolation scheme is controlled by a per-step relative error tolerance parameter, ϵ_{GBS} . In addition, due to the time transformation used in algorithmic regularisation an output time relative tolerance parameter ϵ_t is used to control the accuracy of the iterative solution. Tests of varying ϵ_{GBS} for a fixed value of $\epsilon_t = 10^{-10}$ showed that values of $\epsilon_{\text{GBS}} \lesssim 10^{-7}$ match the reference solution run at $\epsilon_{\text{GBS}} = 10^{-12}$ to a sub-percent level for a typical SMBH binary system. However, following the orbital phase to within one full orbit requires higher precision of $\epsilon_{\text{GBS}} \lesssim 10^{-9}$, which is thus required if one wishes to resolve in detail the post-Newtonian orbital motions of the individual SMBHs, and calculate the resulting GW spectrum (Mannerkoski et al. 2019).

The scalability of the KETJU code depends strongly on the type of problem and in particular on the relative computational cost of the regularised integration compared to the rest of the system. For systems with a relatively low number of particles in the regularised region, the total computational cost is set by the GADGET-4 part, and at high CPU counts the code might even slow down due to suboptimal scaling of the regularised integration. On the contrary, for systems with a high particle load in the region the regularised integrator can scale nearly ideally to a much higher number of CPUs. As the total computational cost is now dominated by the regularised integrator this allows for the use of larger CPU counts than would be sensible for a standard GADGET-4 simulation. In order to avoid a slow-down of the integration at excessive CPU counts, the code automatically limits the number of CPUs allocated to each region based on its particle count.

As a demonstration of the type of problems that can be studied using KETJU we run a set of simulations with multiple galaxy mergers in order to study the formation of cores through core scouring by SMBH binaries (e.g. Milosavljević & Merritt 2001; Merritt 2006; Rantala et al. 2018; Dosopoulou et al. 2021). In the simulations, the multiple SMBHs underwent complex dynamical interactions, with a wide range of resulting merger timescales, determined primarily by the final eccentricities of the SMBH binaries, as expected for GW driven mergers.

All merger remnants displayed depleted stellar cores with tangentially biased central stellar velocity dispersions and core sizes that increased with increasing numbers of progenitor galaxies. The galaxy models were run with rather shallow Hernquist initial density profiles ($\rho \propto r^{-1}$) resulting in core sizes that were larger than the observed cores for similar SMBH masses (Thomas et al. 2016; Dullo et al. 2021). However, the simulations were in good agreement with earlier simulations using similar initial conditions (Rantala et al. 2018). The effect of multiple successive SMBH mergers on the sizes of galactic cores has thus far not been extensively studied, and extending the presented example study to a more complete study with more realistic initial galaxies, multiple merger orbits with varying galactic mass ratios, and the inclusion of SMBH spins and GW recoil kicks would be an obvious interesting application of the presented code (see e.g. Nasim et al. 2021; Dosopoulou et al. 2021 for recent simulation studies).

The public version of GADGET-4, and thus by extension KETJU, does not include models for gas accretion onto SMBHs and the

associated feedback, or models for seeding SMBHs in cosmological simulations. Without such additional models, the presented code is mainly directly applicable for studying SMBH dynamics in gas-poor systems, such as in the mergers of massive elliptical galaxies. For such applications the KETJU code allows running simulations either at higher particle resolution or alternatively enables running a larger set of simulations than has been possible using more conventional high-accuracy N -body codes (e.g. Milosavljević & Merritt 2001; Berczik et al. 2006; Gualandris et al. 2017; Dosopoulou et al. 2021).

However, a variety of sophisticated models for gas cooling, star formation and evolution, as well as gas accretion onto SMBHs and the corresponding feedback exist in the literature and have been implemented in various simulation codes. Adding such models to the public version of KETJU would then allow the code to be used for a wide variety of applications, including studying SMBHs in gas-rich environments or in cosmological simulations with dynamically formed galaxies.

Alternatively, it is possible to use the present code as a basis for adding the KETJU SMBH dynamics to other simulation codes, such as for example AREPO (Springel 2010), RAMSES (Teyssier 2002) or ENZO (Bryan et al. 2014), which already include sophisticated subgrid models for gas, stellar and BH physics. The effort required will depend on how similar the code architecture is to GADGET-4. We also note that the existing SMBH accretion and feedback models need to be improved (Liao et al. 2023), as at $r \lesssim 100$ pc scale separations, where the SMBH binaries can be resolved in KETJU simulations, the preferential accretion from the circumbinary disc is important and will affect the SMBH mass ratio and the strength of the AGN feedback.

While KETJU is not a complete solution to modelling all aspects of how SMBH grow and interact, we have found in our previous studies the code to be a powerful tool for studying SMBHs in certain regimes. Future development of KETJU, or possibly other implementations of similar ideas, will undoubtedly further expand the regimes where it is possible to simultaneously capture the large galactic scales and the small-scale dynamics of SMBHs. We hope that this public release of KETJU will prove useful to the galactic and SMBH simulation communities and result in new advances of our understanding of how SMBHs and galaxies interact.

ACKNOWLEDGEMENTS

MM, AR, PHJ, DI and SL acknowledge the support by the European Research Council via ERC Consolidator Grant KETJU (no. 818930) and the support of the Academy of Finland grant 339127. AR also thanks the support of the University of Helsinki Research Foundation. TN acknowledges support from the Deutsche Forschungsgemeinschaft (DFG, German Research Foundation) under Germany's Excellence Strategy - EXC-2094 - 390783311 from the DFG Cluster of Excellence "ORIGIN". The numerical simulations used computational resources provided by the CSC – IT Center for Science, Finland.

DATA AVAILABILITY

The code presented in this paper is available from <https://www.mv.helsinki.fi/home/phjohans/ketju>. The data from the presented code tests is available upon reasonable request to Peter Johansson.

REFERENCES

- Aarseth S. J., 1999, *PASP*, **111**, 1333
- Amaro-Seoane P., et al., 2023, *Living Reviews in Relativity*, **26**, 2
- Arzoumanian Z., et al., 2018, *ApJ*, **859**, 47
- Begelman M. C., Blandford R. D., Rees M. J., 1980, *Nature*, **287**, 307
- Behroozi P., Wechsler R. H., Hearin A. P., Conroy C., 2019, *MNRAS*, **488**, 3143
- Berczik P., Merritt D., Spurzem R., Bischof H.-P., 2006, *ApJ*, **642**, L21
- Berentzen I., Preto M., Berczik P., Merritt D., Spurzem R., 2009, *ApJ*, **695**, 455
- Binney J., Tremaine S., 2008, *Galactic Dynamics*, second edn. Princeton University Press
- Blanchet L., 2014, *Living Reviews in Relativity*, **17**, 2
- Bonetti M., Sesana A., Haardt F., Barausse E., Colpi M., 2019, *MNRAS*, **486**, 4044
- Booth C. M., Schaye J., 2009, *MNRAS*, **398**, 53
- Bortolas E., Gualandris A., Dotti M., Spera M., Mapelli M., 2016, *MNRAS*, **461**, 1023
- Boylan-Kolchin M., Ma C.-P., 2004, *MNRAS*, **349**, 1117
- Bryan G. L., et al., 2014, *ApJS*, **211**, 19
- Capelo P. R., Volonteri M., Dotti M., Bellovary J. M., Mayer L., Governato F., 2015, *MNRAS*, **447**, 2123
- Cappellari M., et al., 2013, *MNRAS*, **432**, 1709
- Chapon D., Mayer L., Teyssier R., 2013, *MNRAS*, **429**, 3114
- Chen N., Ni Y., Tremmel M., Di Matteo T., Bird S., DeGraf C., Feng Y., 2022, *MNRAS*, **510**, 531
- Choi E., Ostriker J. P., Naab T., Johansson P. H., 2012, *ApJ*, **754**, 125
- Dehnen W., 2014, *Computational Astrophysics and Cosmology*, **1**, 1
- Dosopoulou F., Greene J. E., Ma C.-P., 2021, *ApJ*, **922**, 40
- Dubois Y., Devriendt J., Slyz A., Teyssier R., 2012, *MNRAS*, **420**, 2662
- Duffell P. C., D'Orazio D., Derdzinski A., Haiman Z., MacFadyen A., Rosen A. L., Zrake J., 2020, *ApJ*, **901**, 25
- Dullo B. T., Gil de Paz A., Knapen J. H., 2021, *ApJ*, **908**, 134
- Ebisuzaki T., Makino J., Okumura S. K., 1991, *Nature*, **354**, 212
- Efron B., Tibshirani R. J., 1993, *An Introduction to the Bootstrap*. No. 57 in *Monographs on Statistics and Applied Probability*, Chapman & Hall/CRC, Boca Raton, Florida, USA
- Farris B. D., Duffell P., MacFadyen A. I., Haiman Z., 2014, *ApJ*, **783**, 134
- Ferrarese L., Ford H., 2005, *Space Sci. Rev.*, **116**, 523
- Frigo M., Naab T., Rantala A., Johansson P. H., Neureiter B., Thomas J., Rizzuto F., 2021, *MNRAS*, **508**, 4610
- Fujii M., Iwasawa M., Funato Y., Makino J., 2007, *PASJ*, **59**, 1095
- Graham A. W., Erwin P., Trujillo I., Asensio Ramos A., 2003, *AJ*, **125**, 2951
- Gualandris A., Merritt D., 2008, *ApJ*, **678**, 780
- Gualandris A., Read J. I., Dehnen W., Bortolas E., 2017, *MNRAS*, **464**, 2301
- Gualandris A., Khan F. M., Bortolas E., Bonetti M., Sesana A., Berczik P., Holley-Bockelmann K., 2022, *MNRAS*, **511**, 4753
- Hairer E., Nørsett S., Wanner G., 1993, *Solving Ordinary Differential Equations I: Nonstiff Problems*, second edn. Springer, doi:10.1007/978-3-540-78862-1
- Harfst S., Gualandris A., Merritt D., Mikkola S., 2008, *MNRAS*, **389**, 2
- Hellström C., Mikkola S., 2010, *Celestial Mechanics and Dynamical Astronomy*, **106**, 143
- Hills J. G., Fullerton L. W., 1980, *AJ*, **85**, 1281
- Hirschmann M., Dolag K., Saro A., Bachmann L., Borgani S., Burkert A., 2014, *MNRAS*, **442**, 2304
- Holley-Bockelmann K., Khan F. M., 2015, *ApJ*, **810**, 139
- Iwasawa M., Portegies Zwart S., Makino J., 2015, *Computational Astrophysics and Cosmology*, **2**, 6
- Izquierdo-Villalba D., Sesana A., Bonoli S., Colpi M., 2022, *MNRAS*, **509**, 3488
- Jernigan J. G., Porter D. H., 1989, *ApJS*, **71**, 871
- Johansson P. H., Naab T., Burkert A., 2009a, *ApJ*, **690**, 802
- Johansson P. H., Burkert A., Naab T., 2009b, *ApJ*, **707**, L184
- Karl S. J., Aarseth S. J., Naab T., Haehnelt M. G., Spurzem R., 2015, *MNRAS*, **452**, 2337
- Kelley L. Z., Blecha L., Hernquist L., 2017a, *MNRAS*, **464**, 3131

- Kelley L. Z., Blecha L., Hernquist L., Sesana A., Taylor S. R., 2017b, *MNRAS*, **471**, 4508
- Keppel D., Nichols D. A., Chen Y., Thorne K. S., 2009, *Phys. Rev. D*, **80**, 124015
- Khan F. M., Just A., Merritt D., 2011, *ApJ*, **732**, 89
- Khan F. M., Preto M., Berczik P., Berentzen I., Just A., Spurzem R., 2012, *ApJ*, **749**, 147
- Khan F. M., Fiacconi D., Mayer L., Berczik P., Just A., 2016, *ApJ*, **828**, 73
- Khan F. M., Capelo P. R., Mayer L., Berczik P., 2018, *ApJ*, **868**, 97
- Kormendy J., Ho L. C., 2013, *ARA&A*, **51**, 511
- Kulkarni G., Loeb A., 2012, *MNRAS*, **422**, 1306
- Liao S., et al., 2023, *MNRAS*, **520**, 4463
- Lidov M. L., 1962, *Planet. Space Sci.*, **9**, 719
- Ma L., Hopkins P. F., Kelley L. Z., Faucher-Giguère C.-A., 2023, *MNRAS*, **519**, 5543
- Mannerkoski M., 2022, PhD thesis, University of Helsinki
- Mannerkoski M., Johansson P. H., Pihajoki P., Rantala A., Naab T., 2019, *ApJ*, **887**, 35
- Mannerkoski M., Johansson P. H., Rantala A., Naab T., Liao S., 2021, *ApJ*, **912**, L20
- Mannerkoski M., Johansson P. H., Rantala A., Naab T., Liao S., Rawlings A., 2022, *ApJ*, **929**, 167
- McMillan S. L. W., Aarseth S. J., 1993, *ApJ*, **414**, 200
- Memmesheimer R.-M., Gopakumar A., Schäfer G., 2004, *Phys. Rev. D*, **70**, 104011
- Merritt D., 2006, *ApJ*, **648**, 976
- Merritt D., 2013, *Dynamics and Evolution of Galactic Nuclei*. Princeton University Press
- Mikkola S., Merritt D., 2008, *AJ*, **135**, 2398
- Mikkola S., Tanikawa K., 1999a, *Celestial Mechanics and Dynamical Astronomy*, **74**, 287
- Mikkola S., Tanikawa K., 1999b, *MNRAS*, **310**, 745
- Milosavljević M., Merritt D., 2001, *ApJ*, **563**, 34
- Milosavljević M., Merritt D., Rest A., van den Bosch F. C., 2002, *MNRAS*, **331**, L51
- Mukherjee D., Zhu Q., Trac H., Rodriguez C. L., 2021, *ApJ*, **916**, 9
- Naab T., Ostriker J. P., 2017, *ARA&A*, **55**, 59
- Naab T., Trujillo I., 2006, *MNRAS*, **369**, 625
- Nasim I. T., Gualandris A., Read J. I., Antonini F., Dehnen W., Delorme M., 2021, *MNRAS*, **502**, 4794
- Newman A. B., Ellis R. S., Bundy K., Treu T., 2012, *ApJ*, **746**, 162
- Oshino S., Funato Y., Makino J., 2011, *PASJ*, **63**, 881
- Ostriker E. C., 1999, *ApJ*, **513**, 252
- Pelupessy F. I., van Elteren A., de Vries N., McMillan S. L. W., Drost N., Portegies Zwart S. F., 2013, *A&A*, **557**, A84
- Peters P. C., 1964, *Physical Review*, **136**, 1224
- Peters P. C., Mathews J., 1963, *Physical Review*, **131**, 435
- Pfister H., Volonteri M., Dubois Y., Dotti M., Colpi M., 2019, *MNRAS*, **486**, 101
- Pihajoki P., 2015, *Celestial Mechanics and Dynamical Astronomy*, **121**, 211
- Power C., Navarro J. F., Jenkins A., Frenk C. S., White S. D. M., Springel V., Stadel J., Quinn T., 2003, *MNRAS*, **338**, 14
- Preto M., Tremaine S., 1999, *AJ*, **118**, 2532
- Quinlan G. D., 1996, *New Astron.*, **1**, 35
- Quinlan G. D., Hernquist L., 1997, *New Astron.*, **2**, 533
- Rantala A., Pihajoki P., Johansson P. H., Naab T., Lahén N., Sawala T., 2017, *ApJ*, **840**, 53
- Rantala A., Johansson P. H., Naab T., Thomas J., Frigo M., 2018, *ApJ*, **864**, 113
- Rantala A., Johansson P. H., Naab T., Thomas J., Frigo M., 2019, *ApJ*, **872**, L17
- Rantala A., Pihajoki P., Mannerkoski M., Johansson P. H., Naab T., 2020, *MNRAS*, **492**, 4131
- Rantala A., Naab T., Springel V., 2021, *MNRAS*, **502**, 5546
- Rodriguez C. L., Pattabiraman B., Chatterjee S., Choudhary A., Liao W.-k., Morscher M., Rasio F. A., 2018, *Computational Astrophysics and Cosmology*, **5**, 5
- Roškar R., Fiacconi D., Mayer L., Kazantzidis S., Quinn T. R., Wadsley J., 2015, *MNRAS*, **449**, 494
- Rusli S. P., Erwin P., Saglia R. P., Thomas J., Fabricius M., Bender R., Nowak N., 2013, *AJ*, **146**, 160
- Sahu N., Graham A. W., Davis B. L., 2019, *ApJ*, **876**, 155
- Sijacki D., Springel V., Di Matteo T., Hernquist L., 2007, *MNRAS*, **380**, 877
- Sijacki D., Vogelsberger M., Genel S., Springel V., Torrey P., Snyder G. F., Nelson D., Hernquist L., 2015, *MNRAS*, **452**, 575
- Springel V., 2005, *MNRAS*, **364**, 1105
- Springel V., 2010, *MNRAS*, **401**, 791
- Springel V., Hernquist L., 2003, *MNRAS*, **339**, 289
- Springel V., Di Matteo T., Hernquist L., 2005, *MNRAS*, **361**, 776
- Springel V., Pakmor R., Zier O., Reinecke M., 2021, *MNRAS*, **506**, 2871
- Teyssier R., 2002, *A&A*, **385**, 337
- Thomas J., Saglia R. P., Bender R., Erwin P., Fabricius M., 2014, *ApJ*, **782**, 39
- Thomas J., Ma C.-P., McConnell N. J., Greene J. E., Blakeslee J. P., Janish R., 2016, *Nature*, **532**, 340
- Thorne K. S., Hartle J. B., 1985, *Phys. Rev. D*, **31**, 1815
- Tremmel M., Governato F., Volonteri M., Quinn T. R., 2015, *MNRAS*, **451**, 1868
- Vasiliev E., Antonini F., Merritt D., 2015, *ApJ*, **810**, 49
- Vogelsberger M., Genel S., Sijacki D., Torrey P., Springel V., Hernquist L., 2013, *MNRAS*, **436**, 3031
- Volonteri M., Haardt F., Madau P., 2003, *ApJ*, **582**, 559
- Wang L., Spurzem R., Aarseth S., Nitadori K., Berczik P., Kouwenhoven M. B. N., Naab T., 2015, *MNRAS*, **450**, 4070
- Wang L., Iwasawa M., Nitadori K., Makino J., 2020, *MNRAS*, **497**, 536
- Wetzstein M., Nelson A. F., Naab T., Burkert A., 2009, *ApJS*, **184**, 298
- White S. D. M., Rees M. J., 1978, *MNRAS*, **183**, 341
- Zlochower Y., Lousto C. O., 2015, *Phys. Rev. D*, **92**, 024022
- de Andrade V. C., Blanchet L., Faye G., 2001, *Classical and Quantum Gravity*, **18**, 753

This paper has been typeset from a \LaTeX file prepared by the author.